

Measurements of Cross Sections and Charged Pion Spectra in proton–carbon Interactions at 31 GeV/c

N. Abgrall,¹ A. Aduszkiewicz,² B. Andrieu,³ T. Anticic,⁴ N. Antoniou,⁵ J. Argyriades,¹ A. G. Asryan,⁶ B. Baatar,⁷ A. Blondel,¹ J. Blumer,⁸ M. Bogusz,⁹ L. Boldizsar,¹⁰ A. Bravar,¹ W. Brooks,¹¹ J. Brzychczyk,¹² A. Bubak,¹³ S. A. Bunyatov,⁷ O. Busygina,¹⁴ T. Cetner,⁹ K.-U. Choi,¹⁵ P. Christakoglou,⁵ P. Chung,¹⁶ T. Czopowicz,⁹ N. Davis,⁵ F. Diakonos,⁵ S. Di Luise,¹⁷ W. Dominik,² J. Dumarchez,³ R. Engel,⁸ A. Ereditato,¹⁸ L. S. Esposito,¹⁷ G. A. Feofilov,⁶ Z. Fodor,¹⁰ A. Ferrero,¹ A. Fulop,¹⁰ X. Garrido,⁸ M. Gaździcki,^{19,20} M. Golubeva,¹⁴ K. Grebieszko,⁹ A. Grzeszczuk,¹³ F. Guber,¹⁴ H. Hakobyan,¹¹ T. Hasegawa,²¹ S. Igolkin,⁶ A. S. Ivanov,⁶ Y. Ivanov,¹¹ A. Ivashkin,¹⁴ K. Kadija,⁴ A. Kapoyannis,⁵ N. Katryńska,^{12, a} D. Kielczewska,² D. Kikola,⁹ J.-H. Kim,¹⁵ M. Kirejczyk,² J. Kisiel,¹³ T. Kobayashi,²¹ O. Kochebina,⁶ V. I. Kolesnikov,⁷ D. Kolev,²² V. P. Kondratiev,⁶ A. Korzenev,¹ S. Kowalski,¹³ S. Kuleshov,¹¹ A. Kurepin,¹⁴ R. Lacey,¹⁶ J. Lagoda,²³ A. Laszlo,¹⁰ V. V. Lyubushkin,⁷ M. Mackowiak,⁹ Z. Majka,¹² A. I. Malakhov,⁷ A. Marchionni,¹⁷ A. Marcinek,¹² I. Maris,⁸ V. Marin,¹⁴ T. Matulewicz,² V. Matveev,¹⁴ G. L. Melkumov,⁷ A. Mereaglia,¹⁷ M. Messina,¹⁸ St. Mrówczyński,¹⁹ S. Murphy,¹ T. Nakadaira,²¹ P. A. Naumenko,⁶ K. Nishikawa,²¹ T. Palczewski,²³ G. Palla,¹⁰ A. D. Panagiotou,⁵ W. Peryt,⁹ O. Petukhov,¹⁴ R. Płaneta,¹² J. Pluta,⁹ B. A. Popov,^{7,3} M. Posiadała,² S. Puławski,¹³ W. Rauch,²⁰ M. Ravonel,¹ R. Renfordt,²⁴ A. Robert,³ D. Röhrich,²⁵ E. Rondio,²³ B. Rossi,¹⁸ M. Roth,⁸ A. Rubbia,¹⁷ M. Rybczyński,¹⁹ A. Sadovsky,¹⁴ K. Sakashita,²¹ T. Sekiguchi,²¹ P. Seyboth,¹⁹ M. Shibata,²¹ A. N. Sissakian,^{7, b} E. Skrzypczak,² M. Słodkowski,⁹ A. S. Sorin,⁷ P. Staszal,¹² G. Stefanek,¹⁹ J. Stepaniak,²³ C. Strabel,¹⁷ H. Ströbele,²⁴ T. Susa,⁴ P. Szafflik,¹³ M. Szuba,⁸ M. Tada,²¹ A. Taranenko,¹⁶ R. Tsenov,²² R. Ulrich,⁸ M. Unger,⁸ M. Vassiliou,⁵ V. V. Vechnin,⁶ G. Vesztegombi,¹⁰ A. Wilczek,¹³ Z. Włodarczyk,¹⁹ A. Wojtaszek,¹⁹ J.-G. Yi,¹⁵ I.-K. Yoo,¹⁵ and W. Zipper¹³

(The NA61/SHINE Collaboration)

¹University of Geneva, Geneva, Switzerland

²Faculty of Physics, University of Warsaw, Warsaw, Poland

³LPNHE, University of Paris VI and VII, Paris, France

⁴Rudjer Boskovic Institute, Zagreb, Croatia

⁵University of Athens, Athens, Greece

⁶St. Petersburg State University, St. Petersburg, Russia

⁷Joint Institute for Nuclear Research, Dubna, Russia

⁸Karlsruhe Institute of Technology, Karlsruhe, Germany

⁹Warsaw University of Technology, Warsaw, Poland

¹⁰KFKI Research Institute for Particle and Nuclear Physics, Budapest, Hungary

¹¹Universidad Tecnica Federico Santa Maria, Valparaiso, Chile

¹²Jagiellonian University, Cracow, Poland

¹³University of Silesia, Katowice, Poland

¹⁴Institute for Nuclear Research, Moscow, Russia

¹⁵Pusan National University, Pusan, Republic of Korea

¹⁶State University of New York, Stony Brook, USA

¹⁷ETH, Zurich, Switzerland

¹⁸University of Bern, Bern, Switzerland

¹⁹Jan Kochanowski University in Kielce, Poland

²⁰Fachhochschule Frankfurt, Frankfurt, Germany

²¹High Energy Accelerator Research Organization (KEK), Tsukuba, Ibaraki 305-0801, Japan

²²Faculty of Physics, University of Sofia, Sofia, Bulgaria

²³Soltan Institute for Nuclear Studies, Warsaw, Poland

²⁴University of Frankfurt, Frankfurt, Germany

²⁵University of Bergen, Bergen, Norway

(Dated: October 28, 2018)

Interaction cross sections and charged pion spectra in p+C interactions at 31 GeV/c were measured with the large-acceptance NA61/SHINE spectrometer at the CERN SPS. These data are required to improve predictions of the neutrino flux for the T2K long-baseline neutrino oscillation experiment in Japan. A set of data collected during the first NA61/SHINE run in 2007 with an isotropic graphite target with a thickness of 4% of a nuclear interaction length was used for the analysis. The measured p+C inelastic and production cross sections are $257.2 \pm 1.9 \pm 8.9$ and $229.3 \pm 1.9 \pm 9.0$ mb, respectively. Inclusive production cross sections for negatively and positively charged pions are presented as functions of laboratory momentum in ten intervals of the laboratory

polar angle covering the range from 0 up to 420 mrad. The spectra are compared with predictions of several hadron production models.

PACS numbers: 13.85.Lg,13.85.Hd,13.85.Ni

Keywords: p+C interaction, inelastic cross section, inclusive pion spectra

I. INTRODUCTION

The NA61/SHINE (SPS heavy ion and neutrino experiment) experiment at the CERN Super Proton Synchrotron (SPS) pursues a rich physics program in various fields [1–4]. First, precise hadron production measurements are performed for improving calculations of the neutrino flux in the T2K neutrino oscillation experiment [5], as well as for more reliable simulations of cosmic-ray air showers in the Pierre Auger and KASCADE experiments [6, 7]. Second, p+p, p+Pb and nucleus+nucleus collisions will be studied extensively at SPS energies. A collision energy and system size scan will be performed with the aim to study properties of the onset of deconfinement and searching for the critical point of strongly interacting matter. This paper presents the first NA61/SHINE results on charged pion spectra in p+C interactions at 31 GeV/c, which are needed for an accurate neutrino flux prediction in the T2K experiment. The results are based on the data collected during the first run in 2007. NA61/SHINE is a large-acceptance hadron spectrometer [1]. Its main detector components, software, calibration, and analysis methods were inherited from the NA49 experiment [8, 9].

T2K is a long-baseline neutrino experiment in Japan, which uses a high-intensity neutrino beam produced at J-PARC.¹ It aims to precisely measure the $\nu_\mu \rightarrow \nu_e$ appearance and ν_μ disappearance [5]. In order to generate the neutrino beam a high-intensity 30 GeV (kinetic energy) proton beam impinging on a 90-cm-long graphite target is used, where π and K mesons decaying into (anti)neutrinos are produced. The neutrino fluxes and spectra are then measured both at the near-detector complex, 280 m from the target, and by the Super-Kamiokande (SK) detector located 295 km away from the neutrino source and 2.5° off-axis. Neutrino oscillations are probed by comparing the neutrino flux measured at SK to the predicted one. In order to predict the flux at SK one uses the near-detector measurements and extrapolates them to SK with the help of Monte Carlo simulations. Up to now, these Monte Carlo predictions have been based on hadron production models only. For more precise predictions, which would allow the reduction of systematic uncertainties to the level needed for the T2K physics goals, measurements of pion and kaon

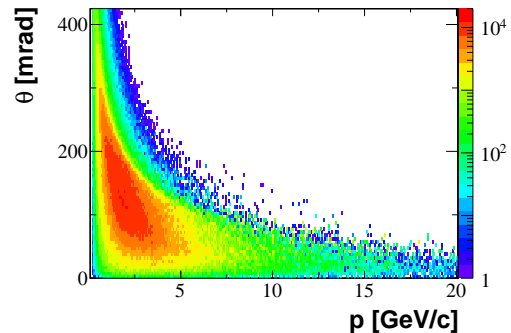


Figure 1: (Color online) The prediction from the T2K beam simulation: the $\{p, \theta\}$ distribution for positively charged pions weighted by the probability that their decay produces a muon neutrino passing through the SK detector.

production off carbon targets are essential [1–3]. The purpose of the NA61/SHINE measurements for T2K is to provide this information at exactly the proton extraction energy of the J-PARC Main Ring synchrotron, namely, 30 GeV kinetic energy (approximately 31 GeV/c momentum). Presently, the T2K neutrino beam-line is set up to focus positively charged hadrons, in such a way that it produces a ν_μ beam. Spectra of positively charged pions presented in this paper constitute directly an essential ingredient in the neutrino flux calculation. The kinematic region of interest for positively charged pions whose daughter muon neutrinos pass through the SK detector is shown in Fig. 1, for the kinematic variables p – the momentum of a given particle and θ – its polar angle in the laboratory frame.

In addition to providing reference data for T2K, precise results on particle production in proton-carbon interactions furnish important input to improve hadronic generators needed for the interpretation of air showers initiated by ultra-high-energy cosmic particles (see, e.g., [10–13]).

The NA61/SHINE data will also allow testing and improvement of existing hadron production models in an intermediate energy region that is not well constrained by measurements at present.

Experimental data on proton-nucleus interactions in the region of momentum of a few tens of GeV/c are rather scarce. Incident proton momenta from 3 up to 12 GeV/c were explored by the HARP Collaboration [14] for a large variety of nuclear targets, including carbon [15]. Almost 40 years ago an experiment was performed at CERN at 24 GeV/c [16]. Several targets were used but the momentum and angular range of produced particles was limited to angles from 17 to 127 mrad and momenta from 4 to 18 GeV/c. Recently the MIPP particle production exper-

^aPresent address: University of Wrocław, Wrocław, Poland.

^bDeceased.

¹ The Japan Proton Accelerator Research Complex organized jointly by JAEA and KEK in Tokai, Japan.

iment at Fermilab presented preliminary results from its first data collected at 120 GeV/ c [17]. Precise measurements of pion production in proton-carbon interactions at 158 GeV/ c are available from the NA49 Collaboration [9].

The paper is organized as follows. In Sec. II the NA61/SHINE experimental set-up is described. Details on the beam, trigger, and event selection are given in Sec. III. Data reconstruction, simulation, and detector performance are described in Sec. IV. Analysis techniques and final results are presented in Secs. V and VI, respectively. These results are compared with hadron production models in Sec. VII. A summary in Sec. VIII closes the paper.

II. THE NA61/SHINE SET-UP

The NA61/SHINE experiment is a large-acceptance hadron spectrometer in the North Area H2 beam-line of the CERN SPS. The schematic layout is shown in Fig. 2 together with the overall dimensions.

The main components of the current detector were constructed and used by the NA49 Collaboration [8]. A set of scintillation and Cherenkov counters as well as beam position detectors (BPDs) upstream of the spectrometer provide timing reference, identification, and position measurements of the incoming beam particles. Details on this system are presented in Sec. III. The main tracking devices of the spectrometer are large-volume time projection chambers (TPCs). Two of them, the vertex TPCs (VTPC-1 and VTPC-2 in Fig. 2), are located in a free gap of 100 cm between the upper and lower coils of the two superconducting dipole magnets. Their maximum combined bending power is 9 T·m. In order to optimize the acceptance of the detector at 31 GeV/ c beam momentum, the magnetic field used during the 2007 data-taking period was set to a bending power of 1.14 T·m. Two large-volume main TPCs (MTPC-L and MTPC-R) are positioned downstream of the magnets symmetrically to the beam line. The TPCs are filled with Ar:CO₂ gas mixtures in proportions 90:10 for VTPCs and 95:5 for MTPCs. The particle identification capability of the TPCs based on measurements of the specific energy loss dE/dx is augmented by time-of-flight measurements (*tof*) using time-of-flight (ToF) detectors. The ToF-L and ToF-R arrays of scintillator pixels have a time resolution of better than 90 ps [8]. Before the 2007 run the experiment was upgraded with a new forward time-of-flight detector (ToF-F) in order to extend the acceptance. The ToF-F consists of 64 scintillator bars with photomultiplier (PMT) readout at both ends resulting in a time resolution of about 115 ps. The target under study is installed 80 cm in front of the VTPC-1. The results presented here were obtained with an isotropic graphite target of dimensions 2.5(W)×2.5(H)×2(L) cm and with a density of $\rho = 1.84$ g/cm³. The target thickness along the beam is equivalent to about 4% of a nuclear interac-

tion length (λ_I).

III. BEAM, TRIGGER AND DATA SAMPLES

A 31 GeV/ c secondary hadron beam is produced from 400 GeV protons extracted from the SPS in slow extraction mode. The beam is transported along the H2 beam-line toward the experiment. Collimators in the beam line are adjusted to get an average beam particle rate of 15 kHz. The setup of beam detectors is illustrated in the inset on Fig. 2. Protons from the secondary hadron beam are identified by two Cherenkov counters, a CEDAR [18] and a threshold counter, labeled C1 and C2, respectively. The CEDAR counter, using a six-fold coincidence, provides positive identification of protons, while the threshold Cherenkov counter, operated at pressure lower than the proton threshold, is used in anti-coincidence in the trigger logic. The fraction of protons in the beam was about 14%. A selection based on signals from Cherenkov counters allowed the identification of beam protons with a purity of about 99%. A consistent value for the purity was found by bending the beam into the TPCs with the full magnetic field and using the dE/dx identification method.

Two scintillation counters S1 and S2 provide beam definition, together with the two veto counters V0 and V1 with a 1-cm-diameter hole, which are collimating the beam on the target. The S1 counter provides also the timing (start time for all counters). Beam protons are then selected by the coincidence $S1 \cdot S2 \cdot \overline{V0} \cdot \overline{V1} \cdot C1 \cdot \overline{C2}$. The trajectory of individual beam particles is measured in a telescope of beam position detectors along the beam line (BPD-1, -2 and -3 in Fig. 2). These counters are small (3×3 cm) proportional chambers with cathode strip readout, providing a resolution of about 200 μ m in two orthogonal directions; see [8] for more details. The beam profile and divergence obtained from the BPD measurements are presented in Fig. 3.

The beam momentum was measured directly in a dedicated run by bending the incoming beam particles into the TPCs with the full magnetic field. The measured beam momentum distribution is shown in Fig. 4. The mean value of 30.75 GeV/ c agrees with the set value of 30.92 GeV/ c within the available precision of setting the beam magnet currents ($\approx 0.5\%$) in the H2 beam-line.

Interactions in the target are selected by an anti-coincidence of the incoming beam protons with a small, 2-cm-diameter, scintillation counter (S4) placed on the beam trajectory between the two vertex magnets (see Fig. 2). This minimum bias trigger is based on the disappearance of the incident proton. A measurement of the interaction cross section is discussed in Sec. VB.

The results presented in this paper are based on the analysis of 667×10^3 proton interaction triggers recorded with the carbon target inserted and 46×10^3 proton interaction triggers recorded with the carbon target removed. Additionally 47×10^3 events were recorded with beam

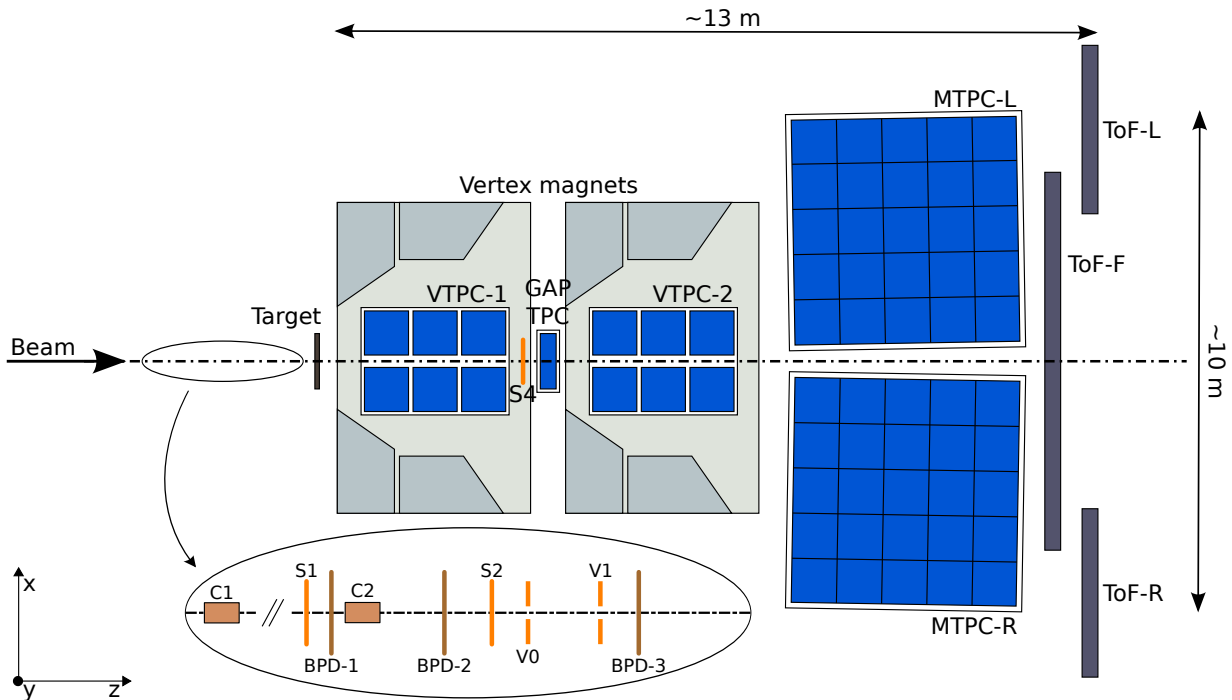


Figure 2: (Color online) The layout of the NA61/SHINE experiment at the CERN SPS (top view, not to scale). The chosen right-handed coordinate system is shown on the plot. The incoming beam direction is along the z axis. The magnetic field bends charged particle trajectories in the x - z (horizontal) plane. The drift direction in the TPCs is along the y (vertical) axis.

proton triggers and 33×10^3 with beam triggers without any beam particle identification.

IV. DATA RECONSTRUCTION, SIMULATION AND DETECTOR PERFORMANCE

A. Calibration

The calibration procedure of the 2007 NA61 data was largely based on the approach developed for the NA49 experiment [8] and consists of several consecutive steps resulting in optimized parameters for

- (i) detector geometry, drift velocity, and residual corrections,
- (ii) magnetic field,
- (iii) time-of-flight measurements, and
- (iv) specific energy loss measurements.

Each step involved reconstruction of the data required to optimize a given set of calibration constants followed by verification procedures. Details of the procedure and quality assessment are presented in Ref. [4]. The quality of detector calibration in quantities relevant for this paper is illustrated in the following subsections.

B. Reconstruction

Reconstruction algorithms used for the analysis described here are based on those developed by the NA49 Collaboration [8]. The main steps of the reconstruction procedure are

- (i) cluster finding in the TPC raw data, and calculation of a cluster center of gravity and total charge,
- (ii) reconstruction of local track segments in each TPC separately,
- (iii) matching of track segments from different TPCs into global tracks,
- (iv) track fitting through the magnetic field and determination of track parameters at the first measured TPC cluster,
- (v) determination of the interaction vertex as the intersection point of the incoming beam particle with the middle target plane,
- (vi) refitting the particle trajectory using the interaction vertex as an additional point and determining the particle momentum at the interaction vertex, and
- (vii) matching of ToF-F hits with the TPC tracks.

An example of a reconstructed event is shown in Fig. 5. One can observe different track topologies, including long tracks hitting the ToF-F.

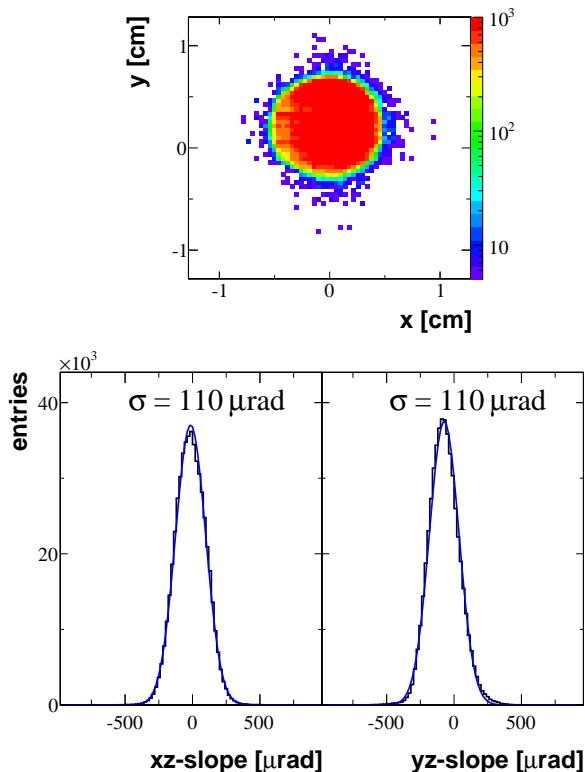


Figure 3: (Color online) *Top*: The beam spot as measured by BPD-3 after the $\bar{V}1$ cut described in the text. *Bottom*: The beam divergence in x and y .

C. Monte Carlo simulation

Simulation of the NA61 detector response used to correct the raw data consists of the following steps (see [19] for more details):

- (i) generation of p+C interactions at 31 GeV/c using the VENUS4.12 [20] model,
- (ii) propagation of outgoing particles through the detector material using the GEANT 3.21 package [21], which takes into account the magnetic field as well as relevant physics processes, such as particle interactions and decays,
- (iii) simulation of the detector response using dedicated NA61 packages which introduce distortions corresponding to all corrections applied to the real data (see Sec. IV A),
- (iv) storage of the simulated events in a file which has the same format as the raw data,
- (v) reconstruction of the simulated events with the same reconstruction chain as used for the real data, and
- (vi) matching of the simulated and reconstructed tracks.

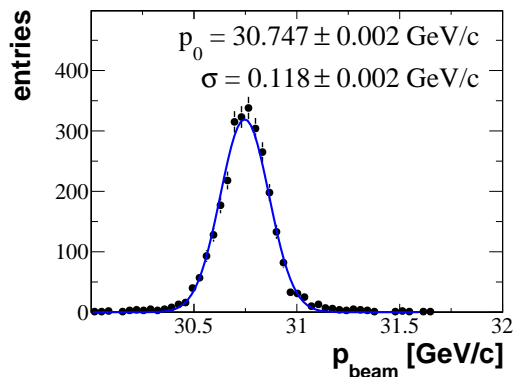


Figure 4: (Color online) The beam momentum distribution measured by the reconstruction of beam particles in the TPCs. Only statistical errors are shown.

Finally, the ratio of the number of reconstructed (matched) tracks in a given (p, θ) bin to the number of generated tracks of the specific particle type in this bin is used as the global correction factor (Sec. V C). Alternatively, flat-phase-space Monte Carlo simulation was used to calculate the same ratio for a given type of primary particle and similar results were obtained within errors for the geometrical acceptance and reconstruction efficiency corrections. The simulation based on the VENUS4.12 model, which has realistic ratios between the different particle species, was used to obtain the corrections due to the admixture of secondary particles e.g., from weak decays of other particles and from secondary interactions. The systematic uncertainties due to the dependence of the corrections on the model are discussed in Sec. V G.

D. Detector performance

The quality of measurements was studied by reconstructing the momentum of beam particles (see Sec. III) and masses of K_S^0 and Λ particles from their V^0 decay topology. As an example the invariant mass distribution of K_S^0 candidates is plotted in Fig. 6. The peak position (0.4976 ± 0.0005 GeV/ c^2) agrees with the known K_S^0 mass. The widths of the K_S^0 and Λ invariant mass peaks are reasonably reproduced by the Monte Carlo simulation, which confirms its validity for the studies presented below.

The track reconstruction efficiency and resolution of kinematic quantities were calculated by matching of simulated and reconstructed tracks. As an example, the reconstruction efficiency as a function of momentum for negatively charged tracks in the polar angle interval $[100, 140]$ mrad is shown in Fig. 7. The momentum resolution $\sigma(p)/p^2$, averaged over different track topologies in the detector, was estimated to be about 2×10^{-3} , 7×10^{-3} , and 3×10^{-2} (GeV/c) $^{-1}$ at $p > 5$ GeV/c, $p = 2$ GeV/c,

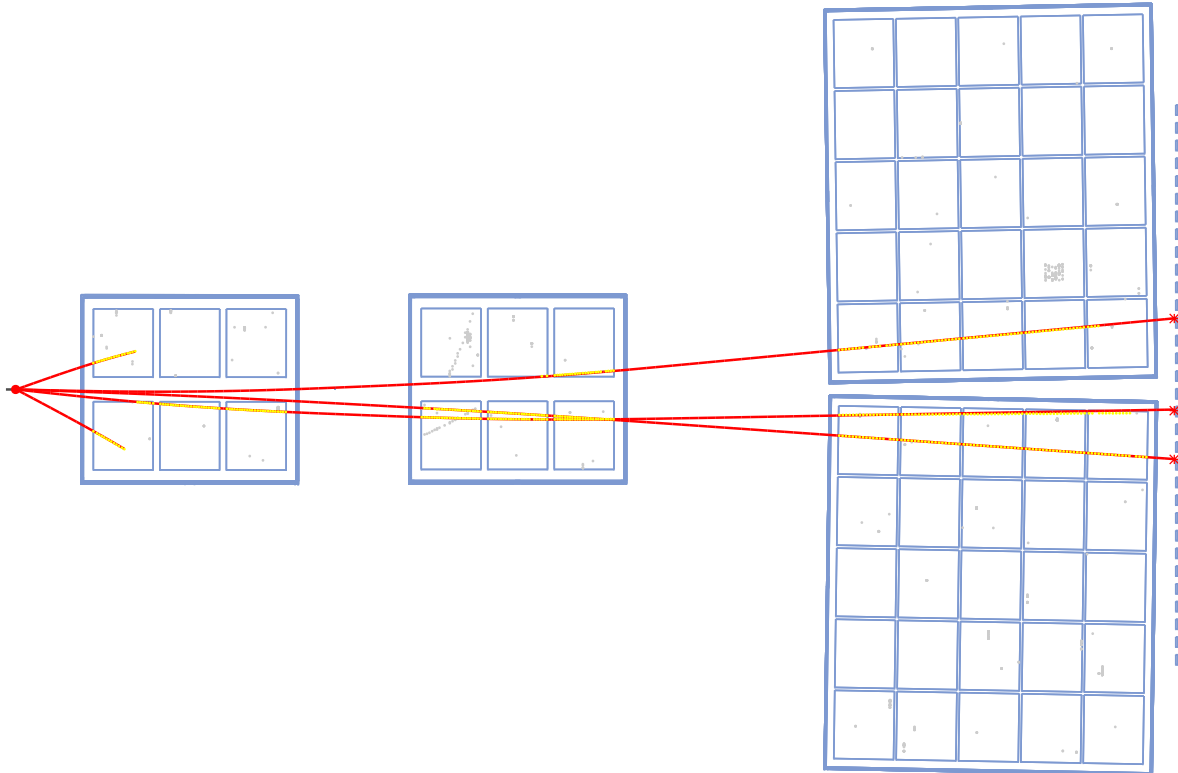


Figure 5: (Color online) Topview (projection to the x - z plane) of a p+C interaction as detected by the four NA61 TPCs and the ToF-F detector (for details see Sec. II and Fig. 2). The red lines correspond to the trajectories of tracks produced in the interaction and reconstructed using the TPC clusters indicated by yellow points. Stars correspond to the reconstructed ToF-F hits.

and $p = 1 \text{ GeV}/c$, respectively. The results depend somewhat on particle production properties, and the quoted numbers refer to negatively charged particles (more than 90% of them are pions) produced by VENUS and passing the track selection cuts described in Sec. V A.

Particle identification was performed based on the energy loss measurements in the TPCs and on the time-of-flight information from the ToF-F detector. The calibrated dE/dx distributions as a function of particle momentum for positively and negatively charged particles are presented in Fig. 8. The Bethe-Bloch parametrization of the mean energy loss, scaled to the experimental data (see Sec. V D), is shown by the curves for positrons (electrons), pions, kaons, protons, and deuterons. The typical achieved dE/dx resolution is 3%-5%; see Fig. 9.

The intrinsic tof resolution of the ToF-F detector is about 115 ps as derived from measurements of tof for particles traversing the overlap region of two adjacent scintillator bars (see Fig. 10). Figure 11 shows distributions of the mass squared m^2 (derived from the tof , fitted momentum, and path length) versus dE/dx (measured in the TPCs) in selected intervals of particle momentum.

The combined m^2 and dE/dx measurements allow us to extract yields of identified particles even in the cross-over region of the Bethe-Bloch curves (1–4 GeV/c momentum range).

The geometrical acceptance of the ToF-F detector is limited to particle momenta above about 0.8 GeV/c . However, in the low-momentum region (less than about 1 GeV/c) the dE/dx information alone is sufficient to distinguish pions from electrons/positrons, kaons, and protons; see Fig. 8.

About 47% of all charged particles produced at the interaction vertex pass the standard TPC track selection cuts (see Sec. V A). In particular, the uninstrumented region around the beam-line in VTPC-1 and VTPC-2 (see Fig. 2) and the magnet apertures lead to a limited acceptance in azimuthal angle. This is illustrated in Fig. 12, where a distribution of all accepted negatively charged particles is shown as a function of azimuthal and polar angles. The fraction of charged particles accepted in the TPCs and in the TPCs plus ToF-F is plotted as a function of momentum and polar angle in Fig. 13. As the azimuthal acceptance varied with the polar angle θ an

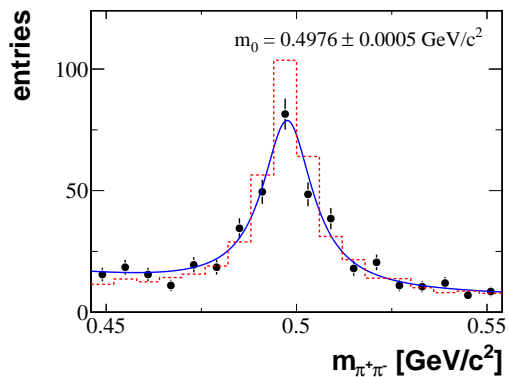


Figure 6: (Color online) Invariant mass distribution of reconstructed K_S^0 candidates. The fitted mean value of the peak is given in the legend. The dashed histogram shows the simulated distribution, which is normalized to the data on the right side of the peak.

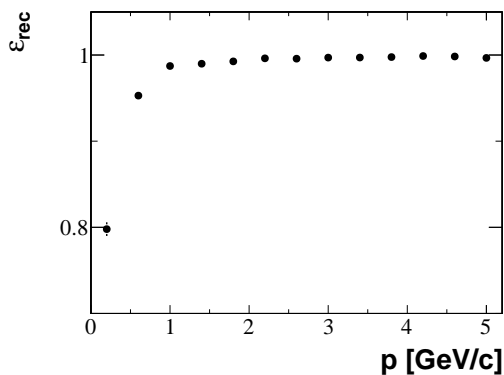


Figure 7: (Color online) Track reconstruction efficiency for negatively charged particles as a function of momentum in the polar angle interval $[100,140]$ mrad.

individual wedge in azimuthal angle ϕ was adjusted for each particular θ bin. Comparing plots in Fig. 13 with Fig. 1, one concludes that the NA61/SHINE acceptance fully covers the phase space region of interest for T2K.

V. ANALYSIS TECHNIQUES

This section presents the procedures used for data analysis. Crucial for this analysis is the identification of the pions produced. Depending on the momentum interval, different approaches were adopted, which led also to different track selection criteria. The task is facilitated for the negatively charged pions by the observation that more than 90% of primary negatively charged particles produced in p+C interactions at this energy are π^- , and thus the analysis of π^- spectra can also be carried out without additional particle identification.

This section starts from a presentation of event and

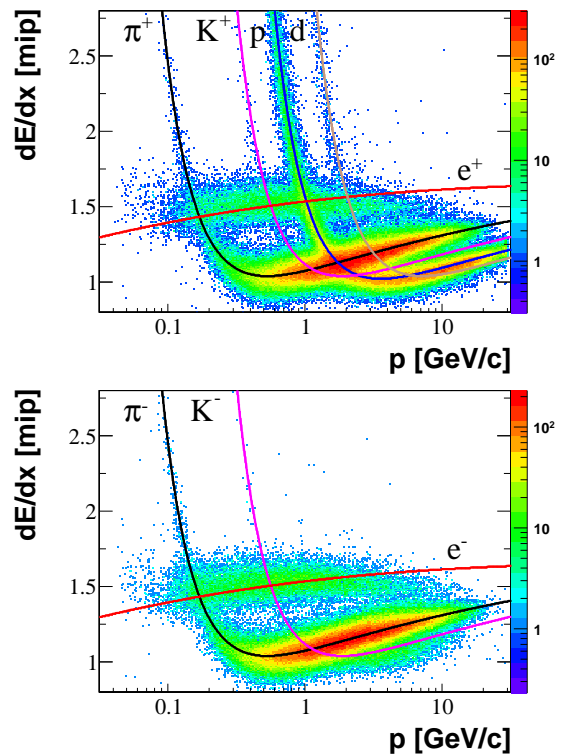


Figure 8: (Color online) Specific energy loss in the TPCs for positively (*top*) and negatively (*bottom*) charged particles as a function of momentum. Curves show parametrizations of the mean dE/dx calculated for different particle species.

track selection cuts. Next, the analysis of interaction cross sections is described [22]. Finally, three analysis methods applied to obtain pion spectra are introduced. These are

- (i) analysis of π^- mesons via measurements of negatively charged particles (*h⁻ analysis* [23]); see Sec. V C;
- (ii) analysis of π^+ and π^- mesons identified via dE/dx measurements in the TPCs (*dE/dx analysis at low momentum* [24]); see Sec. V D; and
- (iii) analysis of π^+ and π^- mesons identified via time-of-flight and dE/dx measurements in the ToF-F and TPCs, respectively (*tof-dE/dx analysis* [25]); see Sec. V E.

Each analysis yields fully corrected pion spectra with independently calculated statistical and systematic errors. The spectra were compared in overlapping phase-space domains to check their consistency. Complementary domains were combined to reach maximum acceptance.

The final results refer to pions (denoted as *primary pions*) produced in p+C interactions at 31 GeV/c by strong interaction processes and in the electromagnetic decays of produced hadrons.

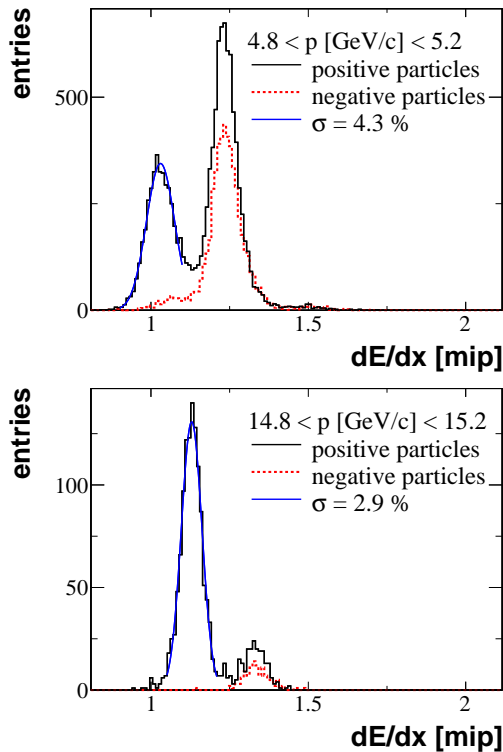


Figure 9: (Color online) The dE/dx distributions for positively (full line) and negatively (dashed line) charged particles at 5 and 15 GeV/ c particle momenta; the momentum bin width is 0.4 GeV/ c .

A. Event and track selection

This section presents event and track selection criteria common for all analysis methods. Selection criteria specific to a given method are described in the corresponding subsection below.

The analysis was based on a sample of 521×10^3 events selected from the total sample of 667×10^3 registered and reconstructed proton interaction triggers recorded with the carbon target inserted. The selected events are required to have signals in each plane of all three BPD detectors with properly reconstructed beam tracks which include measured points on both planes of BPD-3. This criterion essentially removes contamination by interactions upstream of the target. For the event sample with the target removed, the selection reduces the number of events from 46×10^3 to 17×10^3 .

In order to select well-measured tracks in the TPCs as well as to reduce the contamination of tracks from secondary interactions and weak decays the following track selection criteria were applied:

- (i) the track momentum fit at the interaction vertex should have converged,
- (ii) the total number of reconstructed points on a track should be at least 30,

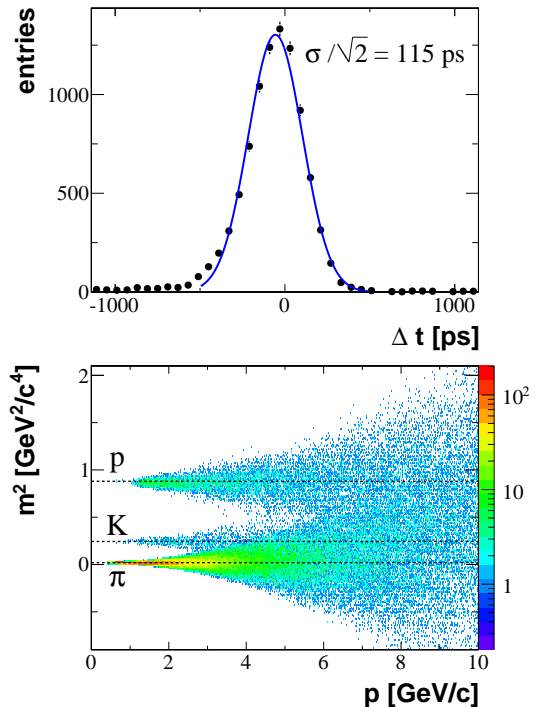


Figure 10: (Color online) *Top*: Distribution of the difference between a particle's time-of-flight measured independently by two overlapping scintillator bars of the ToF-F detector. The width of the distribution is about 160 ps, indicating a tof resolution of about 115 ps for a single measurement. *Bottom*: Mass squared, derived from the ToF-F measurement and the fitted path length and momentum, versus momentum p . The lines show the expected mass squared values for different particles.

- (iii) the sum of the number of reconstructed points in VTPC-1 and VTPC-2 should be at least 12,
- (iv) the ratio of the total number of reconstructed points to the maximum possible number of points derived from the track trajectory with respect to the detector geometry should be larger than 0.5,
- (v) the distance between a track extrapolated to the target plane and the interaction point (impact parameter) should be smaller than 4 cm in both transverse directions separately, and
- (vi) the track azimuthal angle should be within an azimuthal angle wedge around the horizontal plane; the wedge size depends on polar angle and the smallest one ($\pm 20^\circ$ for h^- and dE/dx analyses and $\pm 10^\circ$ for the $tof-dE/dx$ analysis) was used for the largest polar angles; see Fig. 12.

B. Cross section measurements

For normalization and cross section measurements we adopted the same procedure as the one developed by the

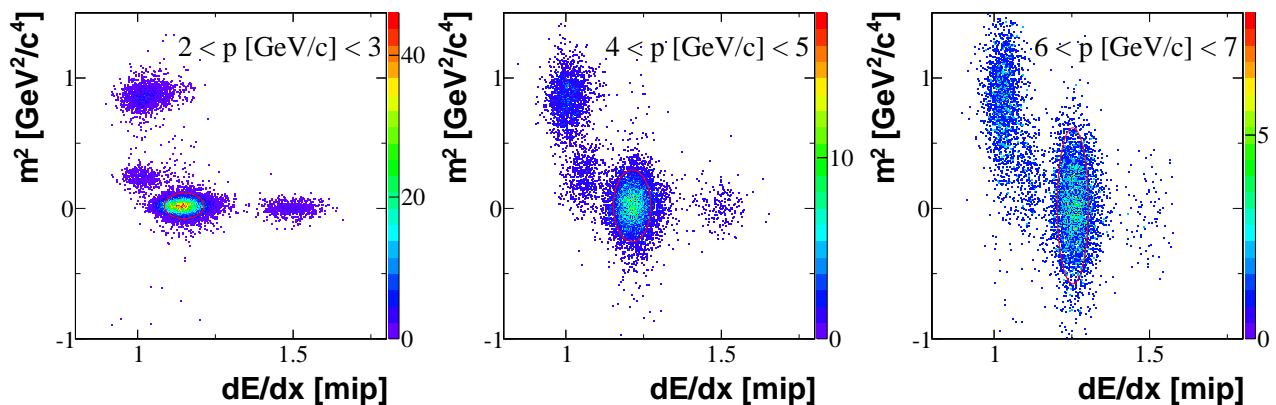


Figure 11: (Color online) Examples of two-dimensional m^2 - dE/dx plots for positively charged particles in three momentum intervals indicated in the panels. 2σ contours around fitted pion peaks are shown. The left and middle plots correspond to the dE/dx cross-over region while the right plot is at such a high momentum that the ToF-F resolution becomes a limiting factor. The combination of both measurements provides close to 100% purity in the pion selection over the whole momentum range.

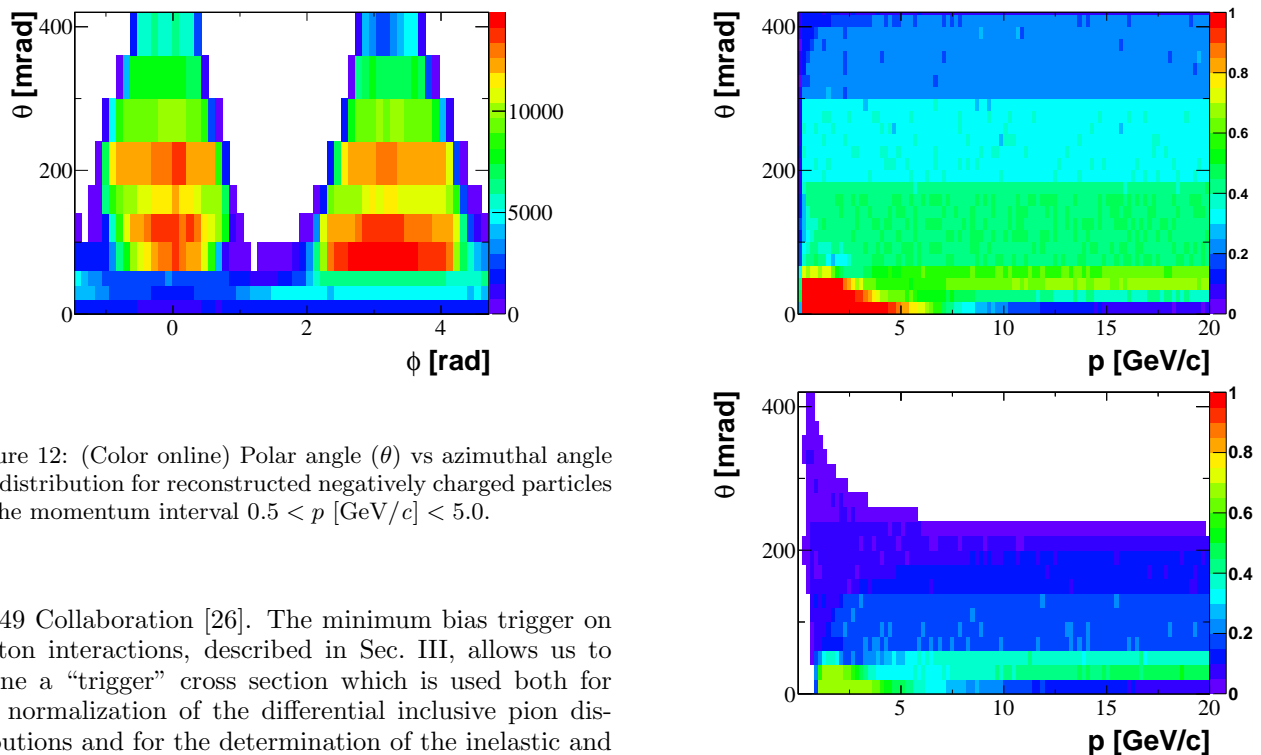


Figure 12: (Color online) Polar angle (θ) vs azimuthal angle (ϕ) distribution for reconstructed negatively charged particles in the momentum interval $0.5 < p$ [GeV/c] < 5.0 .

NA49 Collaboration [26]. The minimum bias trigger on proton interactions, described in Sec. III, allows us to define a “trigger” cross section which is used both for the normalization of the differential inclusive pion distributions and for the determination of the inelastic and production cross sections.

From the numbers of selected interactions, fulfilling the requirements on BPD signals and reconstruction of the proton beam particles as detailed in Sec. V A, we compute an interaction probability of $(6.022 \pm 0.034)\%$ with the carbon target inserted and of $(0.709 \pm 0.007)\%$ with the carbon target removed. These measurements lead to an interaction probability of $(5.351 \pm 0.035)\%$ in the carbon target, taking into account the reduction of the beam intensity in the material along its trajectory. The corresponding “trigger” cross section is $(298.1 \pm 1.9 \pm 7.3)$ mb, after correcting for the exponential beam attenuation in the target. The systematic error on the

Figure 13: (Color online) Fraction of accepted particles as a function of momentum and polar angle, after the track acceptance cuts (see Sec. V A) for negatively charged tracks (*top*), and after an additional ToF-F acceptance cut (see Sec. V E) for positively charged tracks (*bottom*). The first polar angle bin, $[0,20]$ mrad, is fully covered by accepted particles up to 7.6 GeV/c.

“trigger” cross section was conservatively evaluated by comparing this value with the one obtained without any

event selection criteria.

Two classes of processes are considered, inelastic and production interactions. The production processes are defined as those in which new hadrons are produced. The inelastic processes include in addition interactions which result only in disintegration of the target nucleus (quasi-elastic interactions).

The inelastic cross section σ_{inel} was defined as the sum of all processes due to strong p+C interactions except coherent nuclear elastic scattering. Thus it includes interactions with production of new hadrons (production processes) and quasi-elastic interactions which lead only to break up of the carbon nucleus. The inelastic cross section was derived from the “trigger” cross section by applying two corrections:

- (i) subtraction of the contribution from coherent elastic scattering ($47.2 \pm 0.2 \pm 5.0$ mb), i.e., removal of those events in which the incoming beam particle undergoes a large-angle coherent elastic scatter on the carbon nuclei and misses the S4 counter, and
- (ii) addition of the lost inelastic events because of emitted charged particles hitting the S4 counter ($5.7 \pm 0.2 \pm 0.5$ mb for protons and $0.57 \pm 0.02 \pm 0.35$ mb for pions and kaons).

The corrections were calculated based on the GEANT4 [27] simulation (with the QGSP_BERT physics list) of the beam line setup using the measured profile and divergence of the proton beam. The GEANT4 angular distributions for coherent elastic scattering and quasi-elastic scattering, as well as the total inelastic cross section, were cross-checked against available experimental measurements. The largest discrepancy of 7.5% was found for the coherent elastic events in which the scattered proton is outside of the S4 acceptance. This discrepancy was taken into account in the calculation of the systematic error, which includes also uncertainties in other simulation parameters, namely, beam position and divergence, as well as the size of the S4 counter. The total systematic error on the inelastic cross section amounts to 8.9 mb.

The production cross section is determined from the inelastic cross section by subtracting the cross section of quasi-elastic p+C interactions at 31 GeV/c which amounts to 27.9 ± 1.5 (sys) mb according to Glauber model calculations [28].

Details of the cross section analysis procedure can be found in Ref. [22].

C. The h^- analysis

More than 90% of primary negatively charged particles produced in p+C interactions at 31 GeV/c are negatively charged pions. Thus π^- meson spectra can be obtained by subtracting the estimated non-pion contribution from the spectra of negatively charged particles and

additional particle identification is not required. Note that this method is not applicable to the analysis of π^+ meson spectra because of the much larger and unknown contribution of protons and K^+ mesons to all positively charged particles.

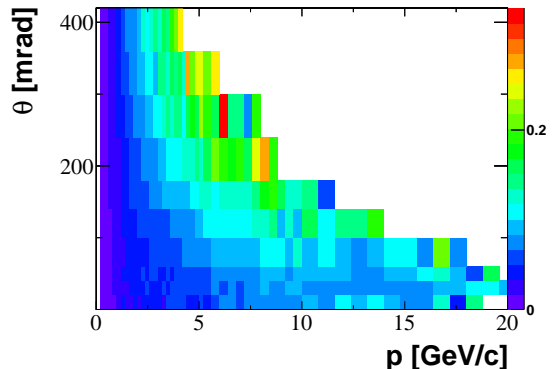


Figure 14: (Color online) The relative contribution of accepted primary K^- and \bar{p} to accepted primary negatively charged pions in different (p, θ) intervals calculated within the VENUS model.

First, spectra of all accepted negatively charged particles were obtained in (p, θ) bins. The event and track selection criteria presented in Sec. V A were applied.

Second, the Monte Carlo simulation described in Sec. IV C was used to calculate corrections for the contribution of electrons and primary K^- and \bar{p} as well as secondary particles from weak decays (feed down), secondary interactions, and photon conversions in the target and the detector material. Furthermore, the corrections include track reconstruction efficiency and resolution as well as losses due to the limited geometrical acceptance of the detector. Bin-by-bin correction factors were calculated as the ratio of all generated primary π^- mesons to all reconstructed and accepted negatively charged particles in a given bin.

Different contributions to the correction factors were studied separately. The losses due to the track reconstruction efficiency and the limited geometrical detector acceptance are shown in Figs. 7 and 13, respectively. The relative contribution of accepted primary K^- and \bar{p} to accepted primary negatively charged pions is presented in Fig. 14. Finally, the relative contribution of accepted electrons and non-primary negatively charged hadrons to accepted primary negatively charged pions is given in Fig. 15. The correction for secondary pions and electrons is largest for small momenta. The former are mainly due to strange particle decays close to the primary vertex; the latter originate mostly from conversion of π^0 decay photons. Uncertainty due to this correction is discussed in Sec. V G.

The inverse correction factor and the geometrical acceptance versus momentum for the polar angle interval [140,180] mrad are shown in Fig. 16 as an example.

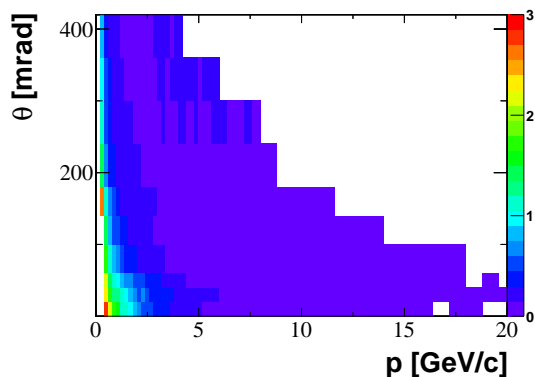


Figure 15: (Color online) The relative contribution of accepted electrons and non-primary negatively charged hadrons to accepted primary negatively charged pions in different (p, θ) intervals calculated within the VENUS model. The low-momentum region where the ratio is larger than 3 is excluded.

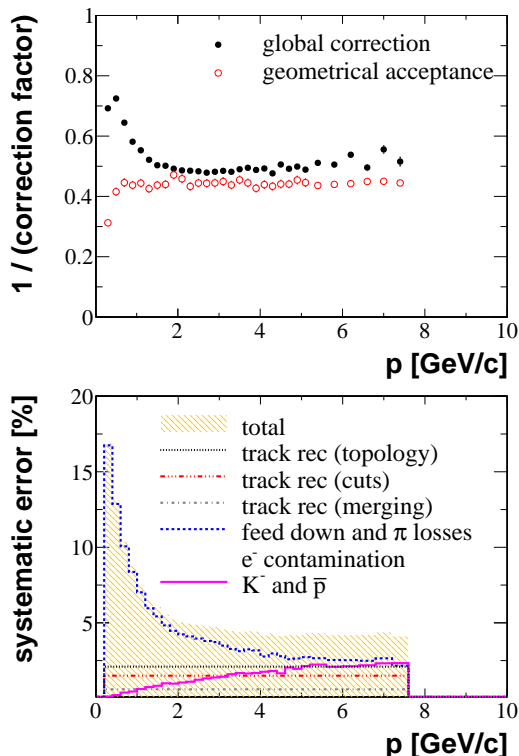


Figure 16: (Color online) Example of momentum dependence of the inverse correction factor and geometrical acceptance (*top*) and systematic errors (*bottom*) for the h^- analysis for negatively charged pions in the polar angle interval $[140, 180]$ mrad. For details concerning systematic uncertainties, see Sec. V G.

D. The dE/dx analysis at low momentum

The analysis of charged pion production at low momentum was done by means of particle identification via measurements of specific energy loss in the TPCs. Measurements of *tof* are not available for low-momentum particles since they do not reach the ToF-F detectors. A reliable identification of π^+ mesons was not possible at momenta above 1 GeV/c where the Bethe-Bloch (BB) curves for pions, kaons, and protons cross each other (see Fig. 8). On the other hand, for π^- mesons, where the contribution of K^- and antiprotons is almost negligible, the dE/dx analysis could be extended in momentum up to 3 GeV/c allowing consistency checks with the other analysis methods in the region of overlap.

The procedure of particle identification, described below, is tailored to the region where a fast change of energy loss with momentum is observed. In order to optimize the parametrization of the BB function, samples of e^\pm , π^\pm , K^\pm , p , and d tracks with reliable particle identification were chosen in the $\beta\gamma$ range from 0.2 up to 100. The dependence of the BB function on $\beta\gamma$ was then fitted to the data using the Sternheimer and Peierls parametrization of Ref. [29]. This function was then used to calculate for every track of a given momentum the expected $(dE/dx)_{BB}$ values for all possible identification hypotheses for comparison with the measured mean $(dE/dx)_{data}$. A small (a few percent) dependence of the mean $(dE/dx)_{data}$ on the track polar angle had to be corrected for.

The identification procedure was performed in (p, θ) bins. Narrow momentum intervals (of 0.1 GeV/c for $p < 1$ GeV/c and 0.2 GeV/c for $1 < p < 3$ GeV/c) were chosen to account for the strong dependence of dE/dx on momentum. The event and track selection criteria presented in Sec. V A were applied. In each (p, θ) bin an unbinned maximum likelihood fit (for details see Ref. [30]) was performed to extract yields of π^+ and π^- mesons. The probability density functions were assumed to be a sum of Gaussian functions for each particle species, centered on $(dE/dx)_{BB}$ with variances derived from data. The dE/dx resolution is a function of the number of measured points and the particle momentum. In the π^+ analysis three independent abundances were fitted (π^+ , K^+ and proton) while in the π^- analysis we were left with only two independent abundances (π^- and K^-). The e^+ and e^- abundances were determined from the total number of particles in the fit.

As an example, the dE/dx distribution for positively charged particles in the momentum bin $[0.7, 0.8]$ GeV/c and angular bin $[180, 240]$ mrad is shown in Fig. 17 compared with the distribution obtained using the fitted parameters.

Finally, the Monte Carlo simulation described in Sec. IV C was used to calculate bin-by-bin corrections for pions from weak decays and interactions in the target and the detector material. The corrections include also track reconstruction efficiency and resolution as well

as losses due to pion decays and the limited geometrical acceptance of the detector. The inverse correction factor and geometrical acceptance versus momentum for the polar angle interval $[140,180]$ mrad is shown in Fig. 18 as an example.

E. The tof - dE/dx analysis

High purity particle identification can be performed by combining the tof and dE/dx information. Moreover, in the momentum range 1–4 GeV/ c , where dE/dx bands for different particle species overlap, particle identification is in general only possible using the tof method; see Figs. 8 and 11 for illustration. The ToF-F detector was designed to cover the necessary acceptance in momentum and polar angle required by the T2K experiment.

First, a particle mass squared, m^2 , was calculated using the tof , momentum, and path length measurements. The m^2 - dE/dx distributions of all accepted positively (and negatively) charged particles were then obtained in each (p, θ) bin. The event and track selection criteria presented in Sec. V A were applied. In addition only tracks which gave a signal in the ToF-F detector were selected. Two independent topologies of tracks, emitted to the left and to the right with respect to the incoming beam direction, have different acceptances. The analysis was performed for each topology separately. When both topologies are present the final result is the weighted average of the two. Momentum-dependent azimuthal angle cuts were applied such that in these angular intervals the detector acceptance was close to 100%. These cuts select tracks with a large number of measured points as well, thus with a high reconstruction efficiency. The averaged

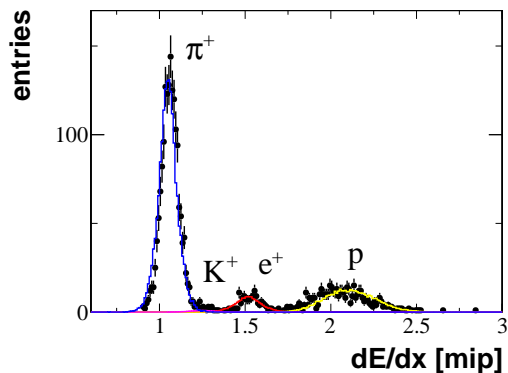


Figure 17: (Color online) The dE/dx distribution for positively charged particles in the momentum bin $[0.7,0.8]$ GeV/ c and angular bin $[180,240]$ mrad compared with the distribution calculated using the fitted relative abundances. A small systematic shift between the fit curves (Gaussian peaks centered on the Bethe-Bloch values) and data is observed. This effect results in a major contribution to the total systematic error in the particle identification procedure.

individual as well as combined global correction factors are shown in Fig. 19 for illustration.

The pion accumulations in these distributions were parametrized by a product of Gaussian functions in m^2 and dE/dx . In each (p, θ) bin the bin-by-bin maximum likelihood method was applied to fit yields of π^+ and π^- mesons. In the fit the signal shapes parametrized in the first step were allowed to vary within narrow limits. The pion yields were calculated summing all particles within 2σ around the fitted pion peak; see Fig. 11. In addition the integral of the fitted function was computed and used for the evaluation of the systematic uncertainty.

Finally, the Monte Carlo simulation described in Sec. IV C was used to calculate corrections for pions from weak decays and interactions in the detector material and target, track reconstruction efficiency and resolution, and losses due to pion decays. The ToF-F detection efficiency was estimated by requiring that a track traversing the ToF-F wall generates a hit in the ToF-F. The ToF-F inefficiency is due also to double hits and readout inefficiencies. The bin-by-bin correction factors for different biases

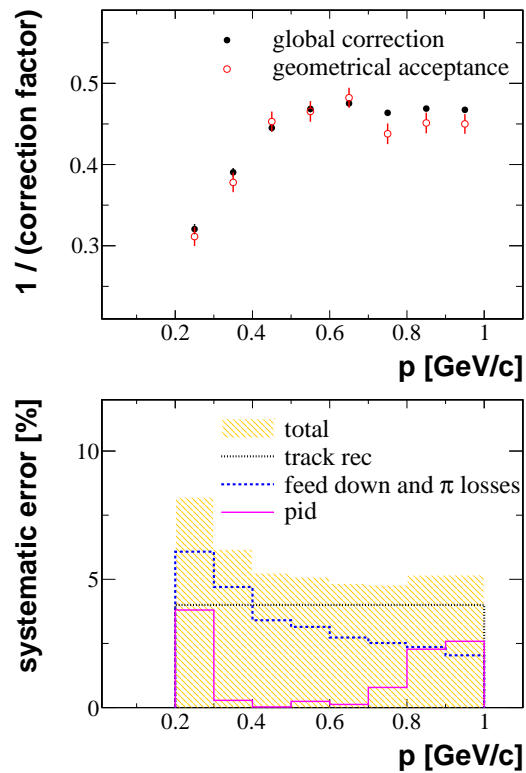


Figure 18: (Color online) Example of the momentum dependence of the inverse correction factor and geometrical acceptance (*top*) and systematic errors (*bottom*) for the dE/dx analysis for positively charged pions in the polar angle interval $[140,180]$ mrad. The small differences between geometrical acceptance and global correction are due to the fact that pion loss and feed down corrections, which are the most important ingredients of the global correction, cancel to a large extent. For details concerning systematic uncertainties see Sec. V G.

were calculated separately and applied to the data. The inverse correction factors versus momentum, total correction factor and geometrical acceptance for the polar angle interval $[40,60]$ mrad are shown in Fig. 19 as an example.

F. Derivation of spectra

The procedures presented in Secs. VC, VD, and VE were used to analyze events with the carbon target inserted (I) and with the carbon target removed (R). The corresponding corrected numbers of π^- and π^+ mesons in p bins and θ intervals are denoted as Δn_α^I and Δn_α^R , where α stands for π^- and π^+ . Note that the same event and track selection criteria as well as corrections discussed in Secs. VC, VD, and VE were used in the analysis of events with the target inserted and removed. The latter events allow us to correct the results for the contribution of out-of-target interactions.

Then, the differential inclusive cross section of π^+ and π^- mesons is calculated as

$$\frac{d\sigma_\alpha}{dp} = \frac{\sigma_{trig}}{1-\epsilon} \left(\frac{1}{N^I} \frac{\Delta n_\alpha^I}{\Delta p} - \frac{\epsilon}{N^R} \frac{\Delta n_\alpha^R}{\Delta p} \right), \quad (1)$$

where

- (i) $\sigma_{trig} = (298.1 \pm 1.9 \pm 7.3)$ mb is the “trigger” cross section as given in Sec. VB,
- (ii) N^I and N^R are the numbers of events selected (see Sec. VA) for the analysis of events with the target inserted and removed, respectively,
- (iii) Δp is the bin size in momentum, and
- (iv) $\epsilon = 0.118 \pm 0.001$ is the ratio of the interaction probabilities for operation with the target removed and inserted.

The correction for the contribution of particles from out-of-target events (the term $\epsilon/N^R \cdot \Delta n_\alpha^R/\Delta p$ in Eq. 1) amounts on average to about 7% and 3% in the first two polar angle intervals. It is smaller than about 2% for polar angle bins above 40 mrad.

The pion spectra normalized to the mean pion multiplicity in production interactions was calculated as

$$\frac{dn_\alpha}{dp} = \frac{1}{\sigma_{prod}} \cdot \frac{d\sigma_\alpha}{dp}, \quad (2)$$

where σ_{prod} is the cross section for production processes.

G. Statistical and systematic errors

Statistical errors on the pion spectra include contributions from the finite statistics of data and from the Monte Carlo simulation used to obtain the correction factors. The Monte Carlo statistics was about ten times larger

than the data statistics and the total statistical errors

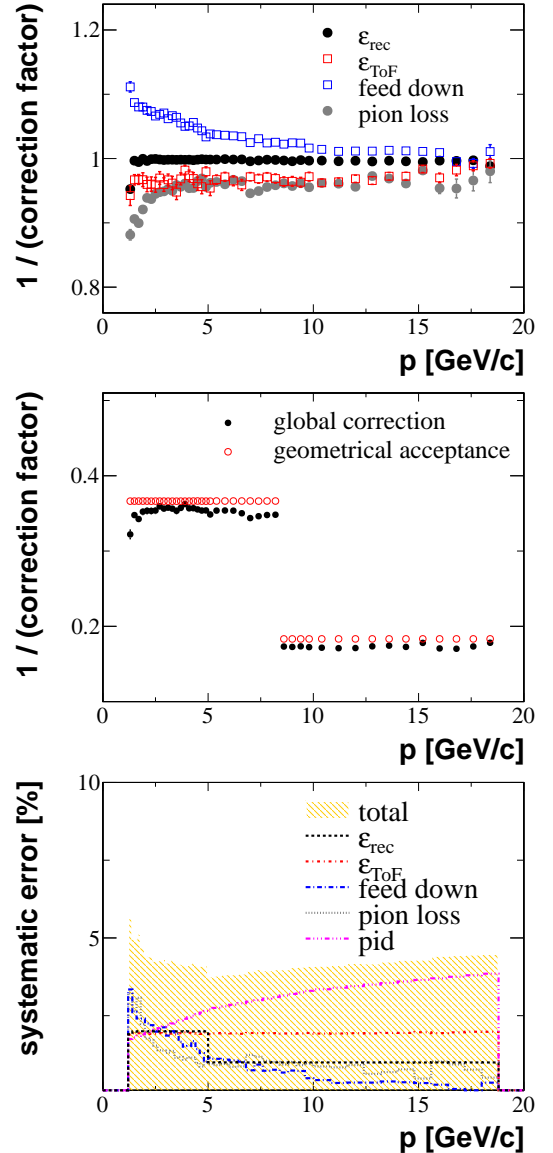


Figure 19: (Color online) Example of momentum dependence of the inverse correction factors (*top*), total inverse correction factor and geometrical acceptance (*middle*), and systematic errors (*bottom*) for the *tof*- dE/dx analysis for positively charged pions in the polar angle interval $[40,60]$ mrad. ϵ_{rec} and ϵ_{ToF} are the efficiencies of the reconstruction and of the ToF-F, respectively. The feed-down correction accounts for pions from weak decays which are reconstructed as primary particles, while the pion loss accounts for pions lost due to decays or secondary interactions. For details concerning systematic uncertainties, see Sec. VG. For the *tof*- dE/dx analysis, within a given theta bin, in addition to the cut on the azimuthal angle, a momentum-dependent selection on the track topology was applied. The purpose of this cut is to select only regions with a flat acceptance along the whole momentum range.

are dominated by the statistical uncertainty of the data.

Systematic errors on the pion spectra were estimated by varying track selection and identification criteria as well as parameters used to calculate the corrections. The following track selection criteria were varied: the minimum number of points measured on the track, the azimuthal angle, and the impact parameter cuts. It was found that the influence of such changes is small as compared to the statistical errors. The accuracy of corrections for acceptance and reconstruction efficiency was checked by comparison of the results obtained with independent track topologies as well as using two different algorithms for merging track segments from different TPCs into global tracks (track merging algorithm). The dominant contributions to the systematic error for all three analysis methods come from the uncertainty in the correction for secondary interactions and for weak decays of strange particles. We assigned an uncertainty of 30% of the correction for both sources. The systematic error due to the admixture of pions from the decays of strange particles reconstructed at the primary vertex depends on the knowledge of strange particle production. The estimate of this error was based on the following.

- (i) Comparison of the number of V^0 decays reconstructed in the data and in the VENUS4.12 model with default parameters.
- (ii) Variation of the strange particle yields in different Monte Carlo generators; for example the K^-/π^- ratio in p+C interactions at 31 GeV/c from FLUKA2008 [31], URQMD1.3.1 [32] and GiBUU1.3.0 [33] (with default value of physics parameters) is 3.73%, 3.67% and 3.35%, respectively; these values can be compared with 4.06% from the VENUS4.12 [20] generator used in this paper for calculation of corrections for pions from weak decays.
- (iii) Comparison of the VENUS4.12 predictions with the measured K^-/π^- and K^+/π^+ ratios from p+B₄C interactions at 24 GeV/c at large momenta and small angles.

In the h^- analysis a 20% uncertainty in the correction for electron admixture to the pion sample was assumed. Examples of systematic errors for all three analyses are presented in the bottom panels of Figs. 16, 18, and 19. Losses of inelastic interactions because an emitted particle hits the S4 counter were estimated to be negligibly small, namely, about 1% or smaller in the relevant phase space for the analysis. The total systematic error was calculated as a sum of different contributions added in quadrature. It does not include the overall uncertainty due to the normalization procedure, namely, 2.5% and 2.3% for the normalization to the inclusive cross section and mean pion multiplicity in production events, respectively. Statistical and systematic uncertainties were added in quadrature in order to calculate the total error. The first quoted error always refers to the statistical and the second to the systematic uncertainty.

VI. RESULTS

This section presents results on inelastic and production cross sections as well as on differential spectra of π^+ and π^- mesons in p+C interactions at 31 GeV/c.

A. Inelastic and production cross sections

The corrections to the “trigger” cross section described in Sec. VB result in a total inelastic cross section of

$$\sigma_{inel} = 257.2 \pm 1.9 \pm 8.9 \text{ mb.}$$

The production cross section was calculated from the inelastic cross section by subtracting the quasi-elastic contribution. The result is

$$\sigma_{prod} = 229.3 \pm 1.9 \pm 9.0 \text{ mb.}$$

The production cross section is compared to previous measurements in Fig. 20. The NA61/SHINE result at 31 GeV/c is consistent with the measurement of Ref. [34] at 20 GeV/c, after subtraction of the quasi-elastic contribution of 30.4 ± 1.9 (sys) mb, and with that of Ref. [35] at 60 GeV/c. The measurements presented in Ref. [36] at different momenta are found to be systematically larger, as was already noted in Ref. [35], where the authors commented “We know of no reason for this discrepancy”. Note that the data from Ref. [36] are about 30 mb higher than other results; if interpreted as measurements of inelastic cross section, they would agree with the other production cross section data, after the correction for the quasi-elastic contribution.

B. Spectra of π^+ and π^- mesons

The π^+ and π^- spectra presented in this section refer to pions produced in strong and electromagnetic processes in p+C interactions at 31 GeV/c.

The spectra normalized to the inclusive cross section are shown in Figs. 21 and 22 for negatively and positively charged pions, respectively. The spectra are presented as functions of particle momentum in ten intervals of the polar angle. Both quantities are calculated in the laboratory system. The chosen binning takes into account the available statistics of the 2007 data sample, detector acceptance, and particle production kinematics.

The spectra obtained by different methods (described in Sec. V) are presented separately. The agreement between them is, in general, better than 10%. Note that data points in the same (p, θ) bin from different analysis methods are statistically correlated as they result from the analysis of the same data set. In order to obtain the final spectra consisting of statistically uncorrelated points, the measurement with the smallest total error was selected. The corresponding numerical values are presented in the Appendix, Table I, and are also available

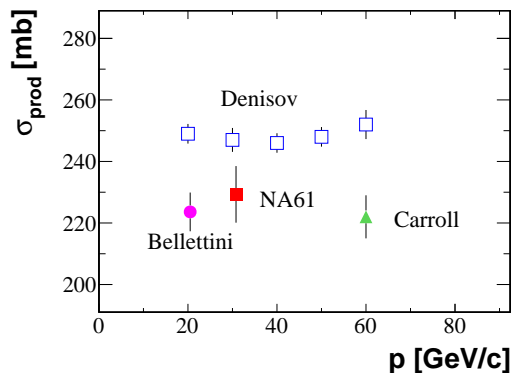


Figure 20: (Color online) Beam momentum dependence of the production cross section for p+C interactions. The NA61/SHINE result (filled square) is compared with previous measurements: Bellettini *et al.* (circle) [34], Carroll *et al.* (triangle) [35] and Denisov *et al.* (open squares) [36]. For the NA61/SHINE point, the error bar indicates statistical and systematic uncertainties added in quadrature. The result from Ref. [34] was recalculated by subtracting from the measured inelastic cross section a quasi-elastic contribution at 20 GeV/ c of 30.4 ± 1.9 (*sys*) mb.

from [37], where the different contributions to systematic uncertainties (see Sec. V G) are given separately.

The final spectra are plotted in Figs. 23 and 24 for π^- and π^+ , respectively, while the corresponding fractional errors are presented in Figs. 25 and 26. For the purpose of a comparison of the data with model predictions, the spectra were normalized to the mean π^\pm multiplicity in all production interactions. This avoids uncertainties due to the different treatment of quasi-elastic interactions in models as well as problems due to the absence of predictions for inclusive cross sections.

The ratio of the final spectra of π^+ and π^- is presented as a function of momentum in Fig. 27. The π^+ to π^- ratio is close to 1 at low momenta and increases with increasing momentum.

VII. COMPARISON TO MODEL PREDICTIONS

As a first application of the measurement presented in this paper, it is interesting to compare the π^- and π^+ spectra in p+C interactions at 31 GeV/ c to the predictions of event generators of hadronic interactions. Models that have been frequently used for the interpretation of cosmic ray data, i.e., VENUS4.12 [20], FLUKA2008 [31], URQMD1.3.1 [32], and GHEISHA2002 [38] were selected. They are part of the CORSIKA [39] framework for the simulation of air showers and are typically used to generate hadron-air interactions at energies below 80 GeV. In order to assure that all relevant settings of the generators are identical to the ones used in air shower simulations, p+C interactions at 31 GeV/ c were simulated within CORSIKA in the so-called *interaction test* mode.

The results are presented in Figs. 23 and 24 for the spectra of π^- and π^+ respectively. As already presented in [40], GHEISHA simulations qualitatively fail to describe the NA61/SHINE measurements at all production angles and momenta (see also, e.g., [10]). The URQMD1.3.1 model qualitatively disagrees with the data only at low momenta ($p < 3$ GeV/ c) and polar angles below about 140 mrad. The VENUS4.12 and FLUKA2008 models follow the data trend in all measured polar angle intervals.

VIII. SUMMARY

This work presents inelastic and production cross sections as well as positively and negatively charged pion spectra in p+C interactions at 31 GeV/ c . These data are essential for precise predictions of the neutrino flux for the T2K long-baseline neutrino oscillation experiment in Japan. Furthermore, they provide important input to improve hadron production models needed for the interpretation of air showers initiated by ultra-high-energy cosmic particles. The measurements were performed with the large-acceptance NA61/SHINE spectrometer at the CERN SPS. A set of data collected with a 4% λ_I isotropic graphite target during the pilot NA61/SHINE run in 2007 was used for the analysis. The p+C inelastic and production cross sections were found to be $257.2 \pm 1.9 \pm 8.9$ and $229.3 \pm 1.9 \pm 9.0$ mb, respectively. Negatively and positively charged pion spectra as a function of laboratory momentum in ten intervals of the polar angle were obtained using three different analysis techniques. The final spectra were compared with predictions of hadron production models.

The data presented in this paper already provide important information for calculating the T2K neutrino flux. Meanwhile, a much larger data set with both the thin (4% λ_I) and the T2K replica carbon targets was recorded in 2009 and 2010 and is presently being analyzed. This will lead to results of higher precision for pions and extend the measurements to other hadron species such as charged kaons, protons, K_S^0 and Λ . The new data will allow a further significant reduction of the uncertainties in the prediction of the neutrino flux in the T2K experiment.

IX. ACKNOWLEDGMENTS

This work was supported by the following funding agencies: the Hungarian Scientific Research Fund (OTKA Grants No. 68506 and No. 79840), the Polish Ministry of Science and Higher Education [Grants No. 667/N-CERN/2010/0, No. N N202 1267 36, No. N N202 287838 (No. PBP 2878/B/H03/2010/38), and No. DWM/57/T2K/2007], the Federal Agency of Education of the Ministry of Education and Science of the Russian Federation (RNP Grant No. 2.2.2.2.1547), the Russian Academy of Sciences and the Russian Founda-

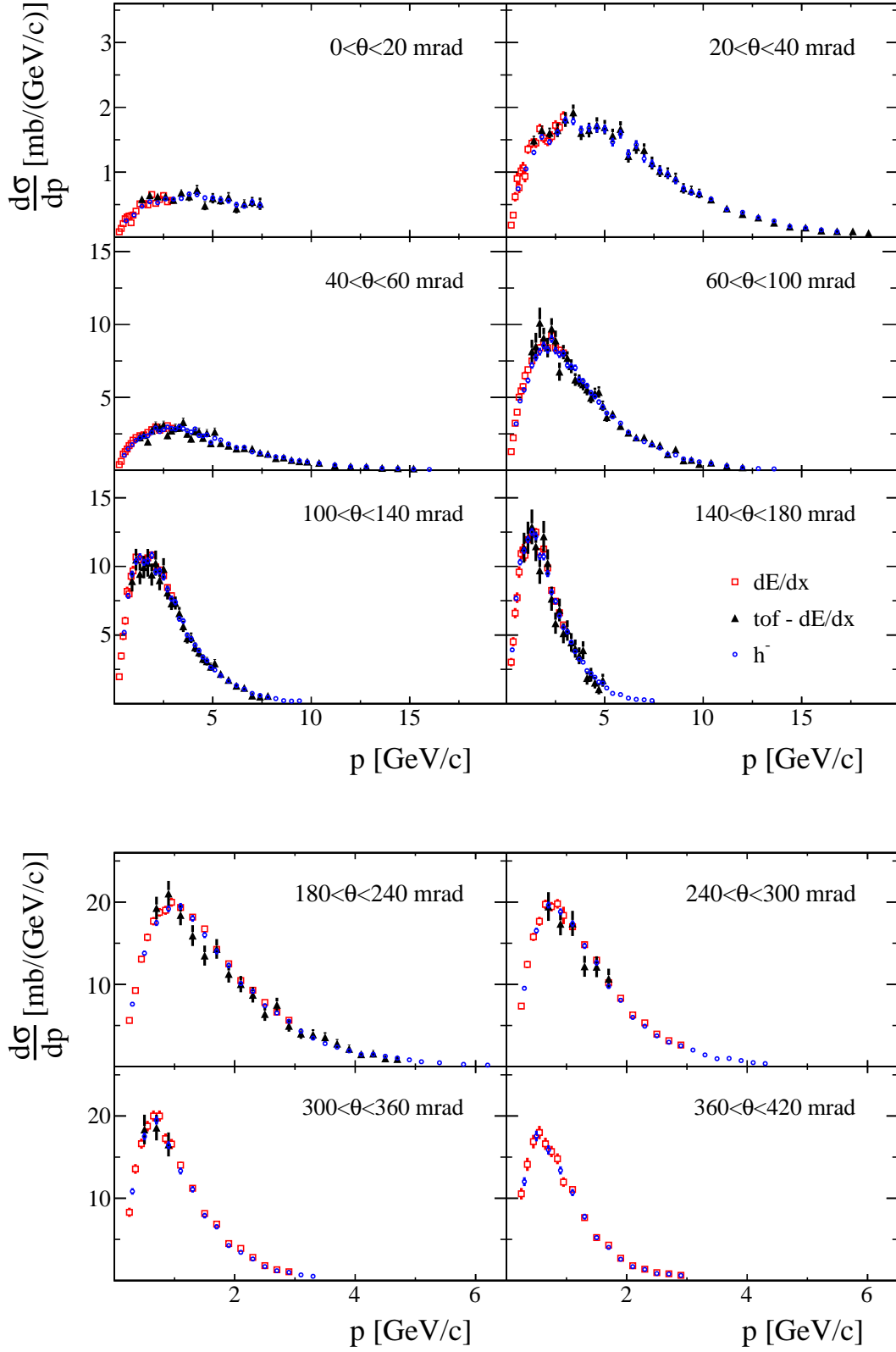


Figure 21: (Color online) Differential cross sections for π^- meson production in p+C interactions at 31 GeV/c. The spectra are presented as a function of laboratory momentum (p) in different intervals of polar angle (θ). Results obtained using three analysis methods are presented by different symbols: blue open circles, h^- analysis; red open squares, dE/dx analysis; and black full triangles, $tof-dE/dx$ analysis. Error bars indicate only statistical uncertainties.

tion for Basic Research (Grants No. 08-02-00018 and No. 09-02-00664), the Ministry of Education, Culture, Sports, Science and Technology, Japan, Grant-in-Aid for Scientific Research (Grants No. 18071005, No. 19034011, No. 19740162, No. 20740160, and No. 20039012), the Toshiko Yuasa Laboratory (France-Japan Particle Physics Laboratory), the Institut National de Physique Nucléaire et Physique des Particules (IN2P3, France), the German Research Foundation (Grant No. GA 1480/2-1), the Swiss National Science Foundation (Investigator-Driven projects and SINERGIA) and the Swiss State Sec-

retariat for Education and Research (FORCE grants). The authors also wish to acknowledge the support provided by the collaborating institutions, in particular, the ETH Zurich (Research Grant No. TH-01 07-3), the University of Bern, and the University of Geneva.

Finally, it is a pleasure to thank the European Organization for Nuclear Research for strong support and hospitality and, in particular, the operating crews of the CERN SPS accelerator and beam lines who made the measurements possible.

-
- [1] N. Antoniou *et al.* (NA49-future Collaboration), Report No. CERN-SPSC-2006-034, 2006.
- [2] N. Antoniou *et al.* (NA61/SHINE Collaboration), Report No. CERN-SPSC-2007-004, 2007.
- [3] N. Antoniou *et al.* (NA61/SHINE Collaboration), Report No. CERN-SPSC-2007-019, 2007.
- [4] N. Abgrall *et al.* (NA61/SHINE Collaboration), Report No. CERN-SPSC-2008-018, 2008.
- [5] Y. Itow *et al.* *The JHF-Kamiokande neutrino project*, arXiv:hep-ex/0106019;
K. Abe *et al.* (T2K Collaboration) *The T2K Experiment*, arXiv:1106.1238v2 [physics.ins-det], *to be published in NIM A*, DOI: 10.1016/j.nima.2011.06.067;
K. Abe *et al.* (T2K Collaboration) *Indication of Electron Neutrino Appearance from an Accelerator-produced Off-axis Muon Neutrino Beam*, Phys. Rev. Lett. **107**, 041801 (2011), arXiv:1106.2822 [hep-ex].
- [6] J. Abraham *et al.* (Pierre Auger Collaboration), Nucl. Instrum. Meth. A **523**, 50 (2004).
- [7] T. Antoni *et al.* (KASCADE Collaboration), Nucl. Instrum. Meth. A **513**, 490 (2003).
- [8] S. Afanasiev *et al.* (NA49 Collaboration), Nucl. Instrum. Meth. A **430**, 257 (1999).
- [9] C. Alt *et al.* (NA49 Collaboration), Eur. Phys. J. **C49**, 897 (2007).
- [10] D. Heck *et al.*, 28th International Cosmic Ray Conference (ICRC 2003), Proceedings edited by T. Kajita, Y. Asaoka, A. Kawachi, Y. Matsubara, M. Sasaki. Tokyo, Japan, Universal Academy Press, 2003. 8v. (Frontiers Science Series, No. 41, 43)
- [11] H.-J. Drescher *et al.*, Astropart. Phys. **21**, 87 (2004).
- [12] C. Meurer *et al.*, Czech. J. Phys. **56** A211 (2006).
- [13] I. C. Maris *et al.*, Nucl. Phys. Proc. Suppl. **196**, 86 (2009).
- [14] M. Apollonio *et al.*, (HARP Collaboration), Phys. Rev. **C80**, 035208 (2009).
- [15] M. G. Catanesi *et al.*, (HARP Collaboration), Astropart. Phys. **29**, 257 (2008).
- [16] T. Eichten *et al.*, Nucl. Phys. B **44**, 333 (1972).
- [17] J. Paley (MIPP Collaboration), AIP Conf. Proc. **981**, 154 (2008).
- [18] C. Bovet, R. Maleyran, L. Piemontese *et al.*, Report No. CERN-YELLOW-82-13.
- [19] N. Abgrall, Ph.D. thesis, University of Geneva, Geneva, Switzerland (in preparation).
- [20] K. Werner, Nucl. Phys. A525, 501c (1991); Phys. Rep. **232**, 87 (1993).
- [21] R. Brun, F. Carminati, GEANT Detector Description and Simulation Tool, CERN Program Library Long Writeup W5013, 1993,
<http://wwwasdoc.web.cern.ch/wwwasdoc/geant/geantall.html>
- [22] C. Strabel, Ph.D. thesis, ETH, Zurich, Switzerland, 2011.
- [23] T. Palczewski, Ph.D. thesis, Soltan Institute for Nuclear Studies, Warsaw, Poland (in preparation).
- [24] M. Posiadala, Ph.D. thesis, University of Warsaw, Warsaw, Poland (in preparation).
- [25] S. Murphy, Ph.D. thesis, University of Geneva, Geneva, Switzerland (in preparation).
- [26] C. Alt *et al.* (NA49 Collaboration), Eur. Phys. J. **C45**, 343 (2006).
- [27] S. Agostinelli *et al.*, (GEANT4 Collaboration), Nucl. Instrum. Methods Phys. Res., Sect. **A506**, (2003) 250.
- [28] R. J. Glauber and G. Matthiae, Nucl. Phys. B **21**, 135 (1970).
- [29] R.M. Sternheimer, R.F. Peierls, Phys. Rev **B3**, 3681 (1971).
- [30] M. Gazdzicki, Nucl. Instrum. Methods Phys. Res., Sect. **A345**, 148 (1994).
- [31] A. Fasso *et al.*, Report No. CERN-2005-10, 2005; G. Battistoni *et al.*, AIP Conf. Proc. **896**, 31, (2007).
- [32] S.M. Bass *et al.*, Prog. Part. Nucl. Phys. **41** 225 (1998); M. Bleicher *et al.*, J. Phys. G: Nucl. Part. Phys. **25**, 1859 (1999).
- [33] <http://gibuu.physik.uni-giessen.de/GiBUU> ;
K. Gallmeister and U. Mosel, Nucl. Phys. A **826**, 151 (2009).
- [34] G. Bellettini *et al.*, Nucl. Phys. **79**, 609 (1966).
- [35] A. S. Carroll *et al.*, Phys. Lett. B **80**, 319 (1979).
- [36] S. P. Denisov *et al.*, Nucl. Phys. B **61**, 62 (1973).
- [37] <https://edms.cern.ch/document/1109626>
- [38] H. Fesefeldt, Aachen Report No. PITHA-85-02 (1985); R.E. Cassell and G. Bower (private communication to D. Heck).
- [39] D. Heck *et al.*, Forschungszentrum Karlsruhe Report No. FZKA-6019, 1998.
- [40] M. Unger, for the NA61/SHINE Collaboration, arXiv:1012.2604 [nucl-ex].

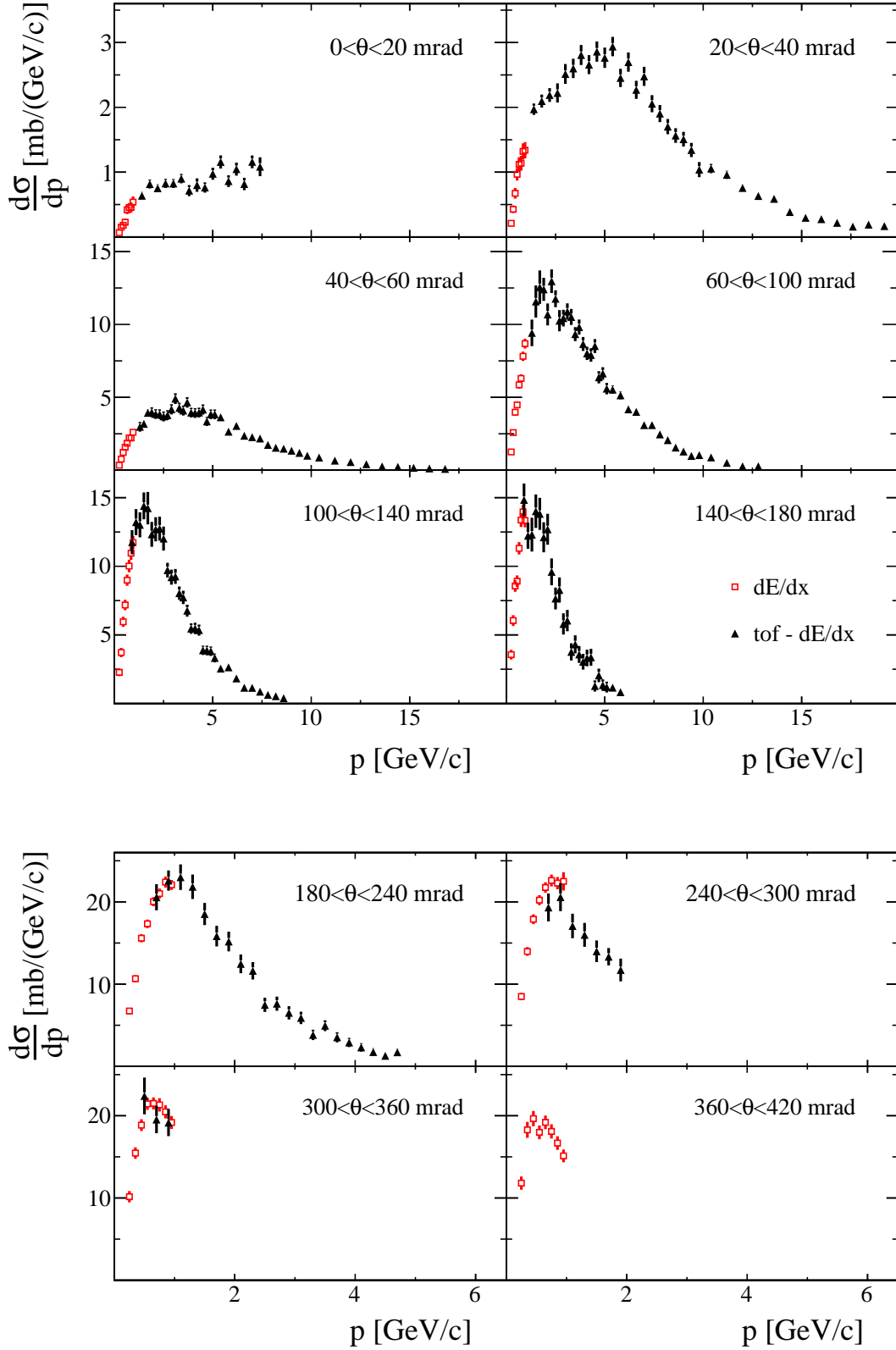


Figure 22: (Color online) Differential cross sections for π^+ meson production in p+C interactions at 31 GeV/c. The spectra are presented as a function of laboratory momentum (p) in different intervals of polar angle (θ). Results obtained using two analysis methods are presented by different symbols: red open squares, dE/dx analysis, and black full triangles, $tof-dE/dx$ analysis. Error bars indicate only statistical uncertainties.

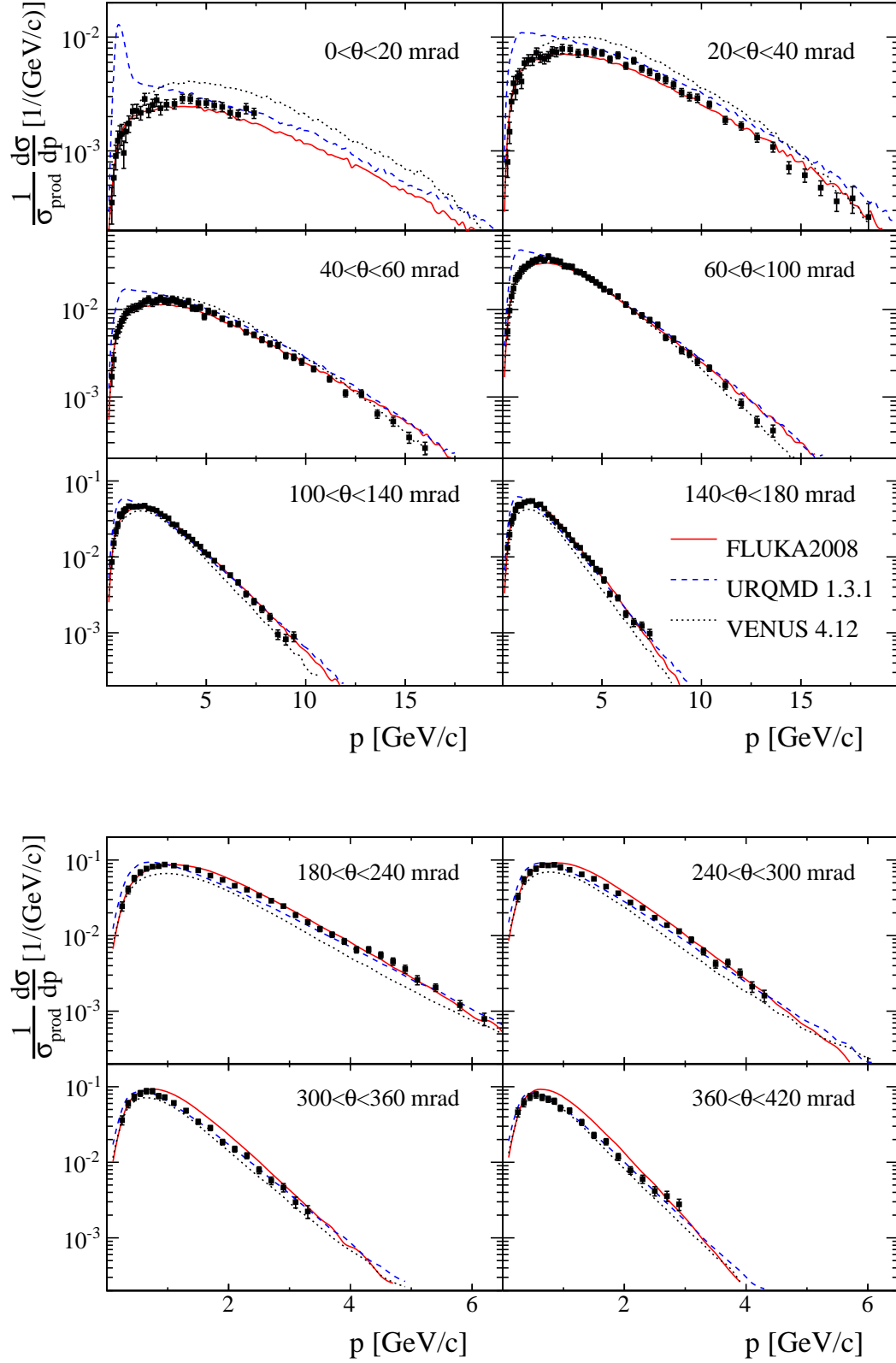


Figure 23: (Color online) Laboratory momentum distributions of π^- mesons produced in production p+C interactions at 31 GeV/c in different intervals of polar angle (θ). The spectra are normalized to the mean π^- multiplicity in all production p+C interactions. Error bars indicate statistical and systematic uncertainties added in quadrature. The overall uncertainty (2.3%) due to the normalization procedure is not shown. Predictions of hadron production models, FLUKA2008 (solid line), URQMD1.3.1 (dashed line), and VENUS4.12 (dotted line), are also indicated.

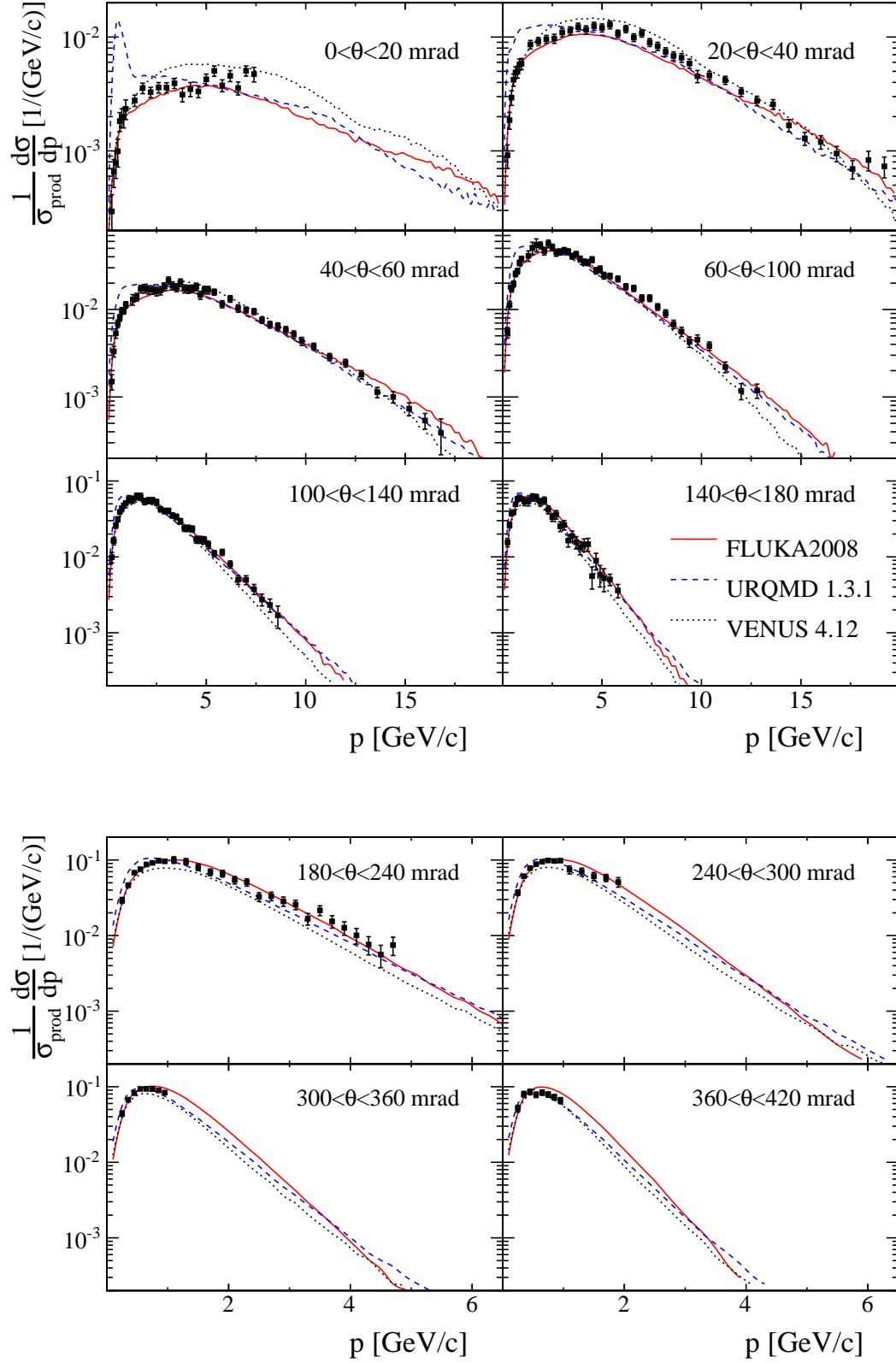


Figure 24: (Color online) Laboratory momentum distributions of π^+ mesons produced in production p+C interactions at 31 GeV/c in different intervals of polar angle (θ). The spectra are normalized to the mean π^+ multiplicity in all production p+C interactions. Error bars indicate statistical and systematic uncertainties added in quadrature. The overall uncertainty (2.3%) due to the normalization procedure is not shown. Predictions of hadron production models, FLUKA2008 (solid line), URQMD1.3.1 (dashed line), and VENUS4.12 (dotted line) are also indicated.

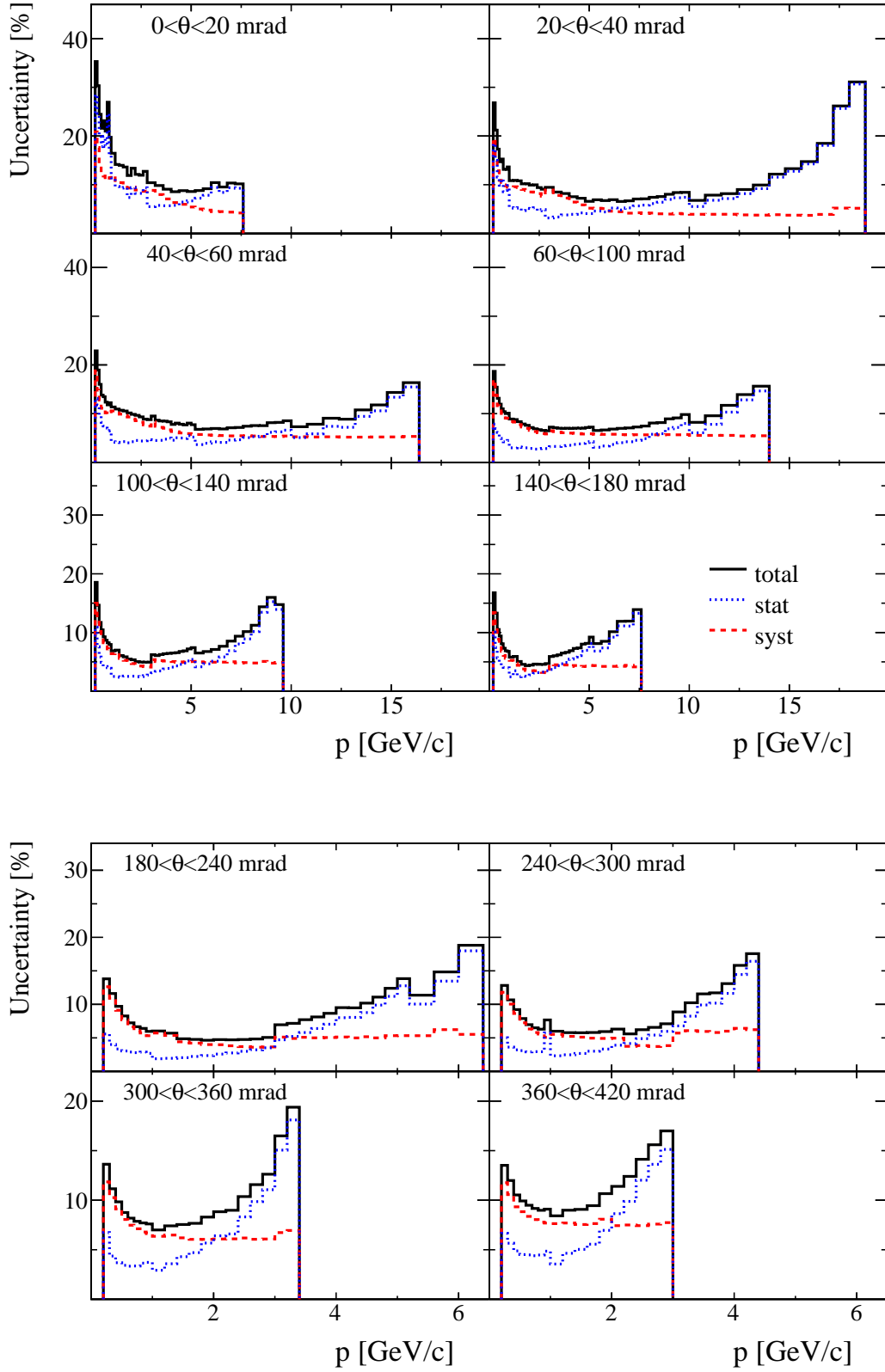


Figure 25: (Color online) Relative uncertainties on the π^- cross sections shown in the same binning as Fig. 23. Statistical (dotted line), systematic (dashed line), and total (solid line) uncertainties are indicated. The overall uncertainty due to the normalization procedure is not shown.

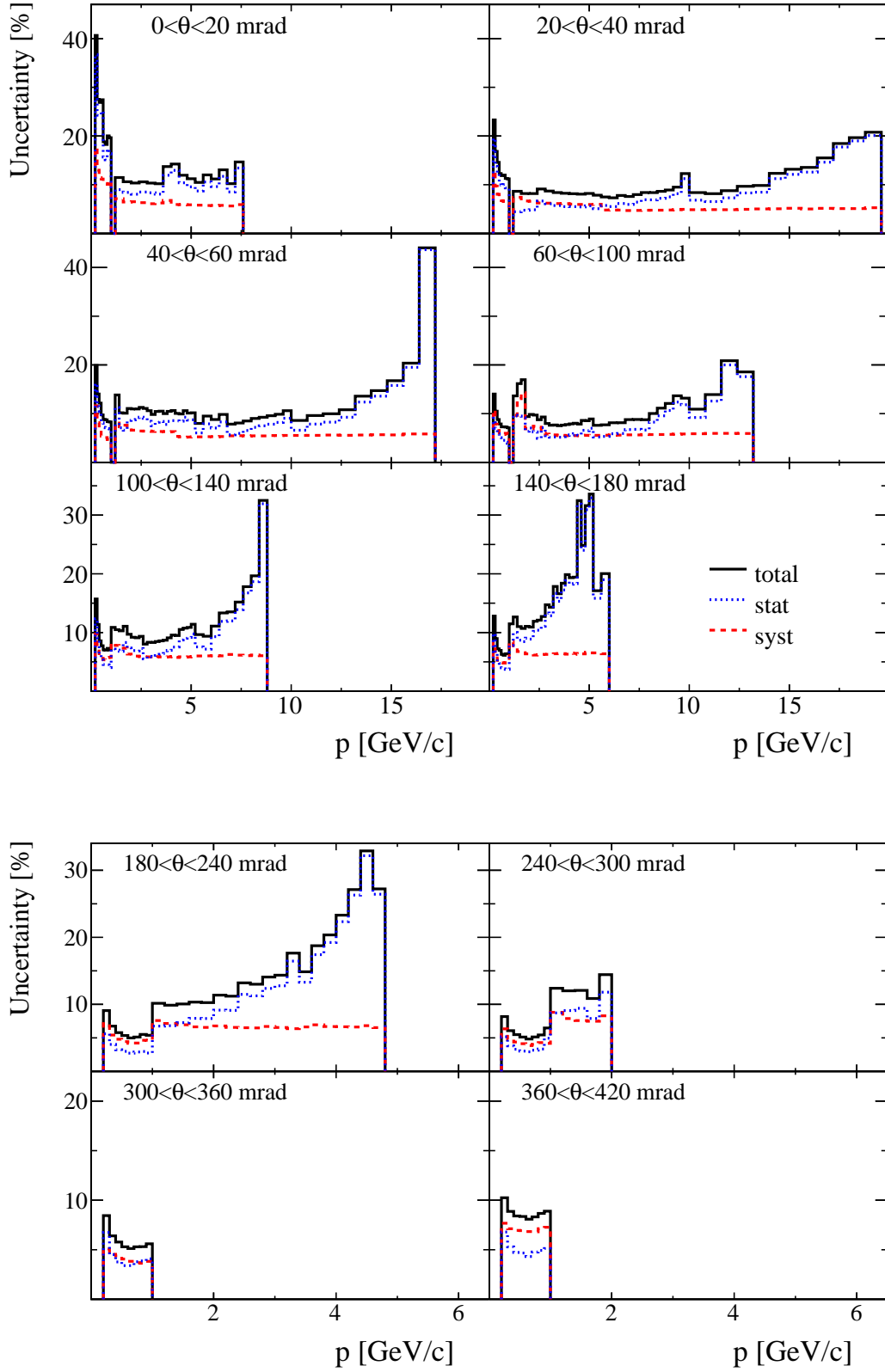


Figure 26: (Color online) Relative uncertainties on the π^+ cross sections shown in the same binning as Fig. 24. Statistical (dotted line), systematic (dashed line), and total (solid line) uncertainties are indicated. The overall uncertainty due to the normalization procedure is not shown.

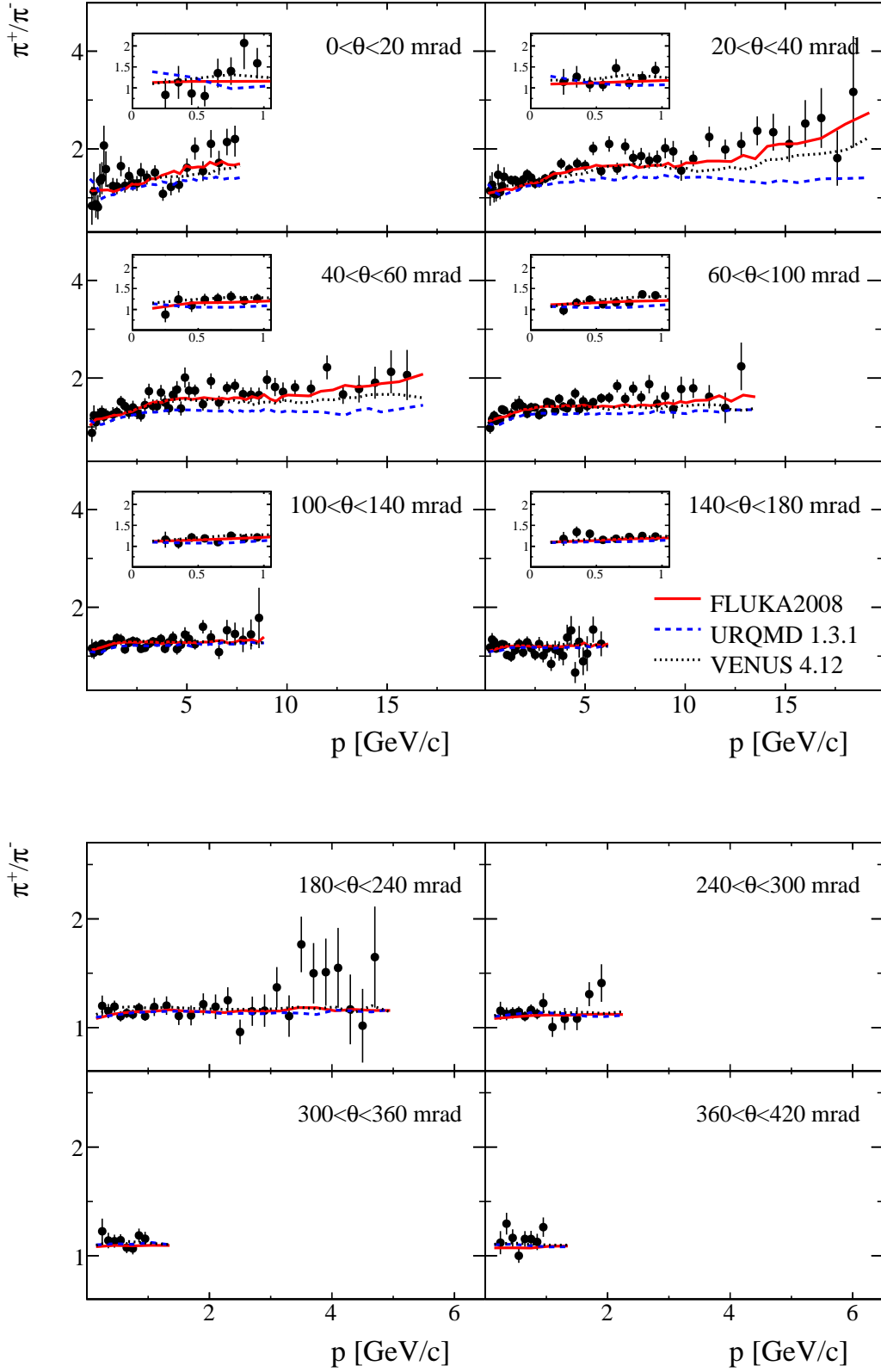


Figure 27: (Color online) The momentum dependence of the π^+ to π^- ratio. Errors are calculated taking into account only statistical uncertainties of the spectra plotted in Figs. 23 and 24. Predictions of hadron production models, FLUKA2008 (solid line), URQMD1.3.1 (dashed line), and VENUS4.12 (dotted line) are also indicated.

Appendix

Table I: The NA61/SHINE results for the differential π^+ and π^- production cross section in the laboratory system, $d\sigma^\pi/dp$, for p+C interactions at 31 GeV/c. Each row refers to a different ($p_{low} \leq p < p_{up}$, $\theta_{low} \leq \theta < \theta_{up}$) bin, where p and θ are the pion momentum and polar angle in the laboratory frame, respectively. The central value as well as the statistical (Δ_{stat}) and systematic (Δ_{sys}) errors are given. The overall uncertainty (2.5%) due to the normalization procedure is not included.

θ_{low} (mrad)	θ_{up}	p_{low} (GeV/c)	p_{up}	$\frac{d\sigma}{dp} \pi^+$ [mb/(GeV/c)]	Δ_{stat}	Δ_{sys}	p_{low} (GeV/c)	p_{up}	$\frac{d\sigma}{dp} \pi^-$ [mb/(GeV/c)]	Δ_{stat}	Δ_{sys}
0	20	0.2	0.3	0.067	0.025	0.012	0.2	0.3	0.081	0.023	0.017
		0.3	0.4	0.151	0.037	0.020	0.3	0.4	0.133	0.033	0.023
		0.4	0.5	0.179	0.044	0.021	0.4	0.5	0.207	0.042	0.028
		0.5	0.6	0.228	0.057	0.025	0.5	0.6	0.282	0.050	0.034
		0.6	0.7	0.419	0.066	0.044	0.6	0.7	0.309	0.062	0.036
		0.7	0.8	0.454	0.069	0.046	0.7	0.8	0.324	0.058	0.036
		0.8	0.9	0.456	0.079	0.046	0.8	0.9	0.220	0.054	0.024
		0.9	1.0	0.537	0.088	0.058	0.9	1.0	0.338	0.054	0.039
							1.0	1.2	0.399	0.045	0.047
		1.2	1.6	0.636	0.057	0.045	1.2	1.4	0.512	0.049	0.053
		1.6	2.0	0.816	0.069	0.053	1.4	1.6	0.516	0.048	0.054
		2.0	2.4	0.752	0.060	0.049	1.6	1.8	0.495	0.047	0.049
		2.4	2.8	0.826	0.070	0.052	1.8	2.0	0.655	0.048	0.061
		2.8	3.2	0.825	0.069	0.050	2.0	2.2	0.519	0.049	0.049
		3.2	3.6	0.900	0.073	0.056	2.2	2.4	0.581	0.048	0.052
		3.6	4.0	0.715	0.085	0.048	2.4	2.6	0.639	0.053	0.055
		4.0	4.4	0.80	0.10	0.05	2.6	2.8	0.543	0.051	0.047
		4.4	4.8	0.763	0.079	0.045	2.8	3.2	0.584	0.032	0.052
		4.8	5.2	0.975	0.093	0.057	3.2	3.6	0.593	0.034	0.047
		5.2	5.6	1.16	0.10	0.07	3.6	4.0	0.662	0.038	0.047
		5.6	6.0	0.862	0.091	0.049	4.0	4.4	0.655	0.038	0.041
		6.0	6.4	1.05	0.10	0.06	4.4	4.8	0.604	0.039	0.036
		6.4	6.8	0.817	0.096	0.047	4.8	5.2	0.604	0.040	0.033
		6.8	7.2	1.159	0.099	0.065	5.2	5.6	0.577	0.042	0.029
		7.2	7.6	1.08	0.15	0.06	5.6	6.0	0.558	0.044	0.027
							6.0	6.4	0.498	0.047	0.022
							6.4	6.8	0.477	0.040	0.021
							6.8	7.2	0.541	0.051	0.024
							7.2	7.6	0.492	0.046	0.021
20	40	0.2	0.3	0.210	0.041	0.027	0.2	0.3	0.183	0.034	0.036
		0.3	0.4	0.427	0.059	0.041	0.3	0.4	0.337	0.051	0.051
		0.4	0.5	0.674	0.082	0.054	0.4	0.5	0.621	0.072	0.080
		0.5	0.6	0.967	0.096	0.069	0.5	0.6	0.901	0.089	0.098
		0.6	0.7	1.12	0.11	0.08	0.6	0.7	0.761	0.085	0.080
		0.7	0.8	1.14	0.11	0.07	0.7	0.8	1.02	0.09	0.10
		0.8	0.9	1.32	0.12	0.08	0.8	0.9	1.07	0.09	0.10
		0.9	1.0	1.34	0.13	0.08	0.9	1.0	0.936	0.092	0.089
							1.0	1.2	1.35	0.07	0.13
		1.2	1.6	1.97	0.09	0.15	1.2	1.4	1.45	0.08	0.14
		1.6	2.0	2.10	0.10	0.14	1.4	1.6	1.45	0.08	0.14
		2.0	2.4	2.19	0.11	0.14	1.6	1.8	1.67	0.08	0.15
		2.4	2.8	2.22	0.15	0.14	1.8	2.0	1.53	0.08	0.13
		2.8	3.2	2.52	0.15	0.16	2.0	2.2	1.48	0.08	0.13
		3.2	3.6	2.60	0.15	0.16	2.2	2.4	1.55	0.08	0.13
		3.6	4.0	2.81	0.15	0.17	2.4	2.6	1.72	0.08	0.14
		4.0	4.4	2.66	0.15	0.16	2.6	2.8	1.69	0.08	0.13
		4.4	4.8	2.86	0.16	0.17	2.8	3.2	1.80	0.06	0.16
		4.8	5.2	2.77	0.16	0.16	3.2	3.6	1.78	0.06	0.14

Continued on next page

θ_{low}	θ_{up}	p_{low}	p_{up}	$\frac{d\sigma}{dp} \pi^+$	Δ_{stat}	Δ_{sys}	p_{low}	p_{up}	$\frac{d\sigma}{dp} \pi^-$	Δ_{stat}	Δ_{sys}
(mrad)	(GeV/c)	(GeV/c)	(GeV/c)	[mb/(GeV/c)]	[mb/(GeV/c)]	[mb/(GeV/c)]	(GeV/c)	(GeV/c)	[mb/(GeV/c)]	[mb/(GeV/c)]	[mb/(GeV/c)]
		5.2	5.6	2.94	0.15	0.18	3.6	4.0	1.65	0.06	0.12
		5.6	6.0	2.45	0.14	0.12	4.0	4.4	1.68	0.07	0.11
		6.0	6.4	2.70	0.15	0.13	4.4	4.8	1.683	0.071	0.099
		6.4	6.8	2.27	0.14	0.11	4.8	5.2	1.667	0.068	0.086
		6.8	7.2	2.48	0.15	0.12	5.2	5.6	1.463	0.067	0.076
		7.2	7.6	2.06	0.13	0.10	5.6	6.0	1.587	0.070	0.081
		7.6	8.0	1.90	0.13	0.09	6.0	6.4	1.284	0.067	0.059
		8.0	8.4	1.70	0.12	0.08	6.4	6.8	1.423	0.068	0.063
		8.4	8.8	1.56	0.11	0.07	6.8	7.2	1.209	0.063	0.050
		8.8	9.2	1.51	0.11	0.07	7.2	7.6	1.132	0.064	0.048
		9.2	9.6	1.34	0.11	0.07	7.6	8.0	1.027	0.060	0.042
		9.6	10.0	1.04	0.12	0.05	8.0	8.4	0.967	0.059	0.040
		10.0	10.8	1.055	0.072	0.051	8.4	8.8	0.872	0.056	0.035
		10.8	11.6	0.959	0.063	0.047	8.8	9.2	0.749	0.052	0.030
		11.6	12.4	0.756	0.055	0.037	9.2	9.6	0.688	0.050	0.028
		12.4	13.2	0.632	0.053	0.031	9.6	10.0	0.667	0.049	0.027
		13.2	14.0	0.588	0.050	0.030	10.0	10.8	0.586	0.032	0.023
		14.0	14.8	0.384	0.043	0.019	10.8	11.6	0.427	0.029	0.017
		14.8	15.6	0.295	0.036	0.015	11.6	12.4	0.380	0.027	0.015
		15.6	16.4	0.275	0.035	0.014	12.4	13.2	0.301	0.025	0.011
		16.4	17.2	0.217	0.032	0.011	13.2	14.0	0.248	0.023	0.009
		17.2	18.0	0.159	0.028	0.008	14.0	14.8	0.164	0.019	0.006
		18.0	18.8	0.191	0.036	0.010	14.8	15.6	0.140	0.018	0.005
		18.8	19.6	0.168	0.034	0.009	15.6	16.4	0.109	0.016	0.004
							16.4	17.2	0.083	0.015	0.003
							17.2	18.0	0.088	0.023	0.005
							18.0	18.8	0.060	0.018	0.003
40	60	0.2	0.3	0.344	0.056	0.040	0.2	0.3	0.391	0.051	0.074
		0.3	0.4	0.763	0.087	0.062	0.3	0.4	0.616	0.073	0.091
		0.4	0.5	1.22	0.13	0.08	0.4	0.5	1.12	0.11	0.14
		0.5	0.6	1.58	0.13	0.08	0.5	0.6	1.28	0.10	0.14
		0.6	0.7	1.85	0.13	0.09	0.6	0.7	1.47	0.11	0.16
		0.7	0.8	2.22	0.16	0.11	0.7	0.8	1.69	0.12	0.17
		0.8	0.9	2.22	0.15	0.10	0.8	0.9	1.83	0.12	0.18
		0.9	1.0	2.60	0.18	0.12	0.9	1.0	2.07	0.13	0.21
							1.0	1.2	2.24	0.09	0.24
		1.2	1.4	2.98	0.33	0.24	1.2	1.4	2.37	0.10	0.24
		1.4	1.6	3.18	0.23	0.23	1.4	1.6	2.43	0.10	0.24
		1.6	1.8	3.94	0.26	0.30	1.6	1.8	2.59	0.11	0.25
		1.8	2.0	3.97	0.34	0.28	1.8	2.0	2.79	0.11	0.26
		2.0	2.2	3.85	0.34	0.25	2.0	2.2	2.98	0.13	0.27
		2.2	2.4	3.84	0.34	0.25	2.2	2.4	2.75	0.12	0.23
		2.4	2.6	3.69	0.34	0.24	2.4	2.6	2.86	0.13	0.24
		2.6	2.8	3.78	0.34	0.24	2.6	2.8	3.06	0.14	0.24
		2.8	3.0	4.18	0.35	0.27	2.8	3.0	2.88	0.13	0.21
		3.0	3.2	4.91	0.37	0.31	3.0	3.2	2.83	0.13	0.24
		3.2	3.4	4.28	0.35	0.27	3.2	3.4	2.99	0.13	0.22
		3.4	3.6	4.09	0.34	0.26	3.4	3.6	2.87	0.13	0.21
		3.6	3.8	4.65	0.36	0.29	3.6	3.8	2.73	0.13	0.19
		3.8	4.0	3.95	0.33	0.25	3.8	4.0	2.64	0.13	0.18
		4.0	4.2	3.92	0.34	0.25	4.0	4.2	2.84	0.13	0.18
		4.2	4.4	3.96	0.34	0.21	4.2	4.4	2.39	0.12	0.15
		4.4	4.6	4.16	0.35	0.22	4.4	4.6	2.36	0.12	0.14
		4.6	4.8	3.35	0.31	0.17	4.6	4.8	2.43	0.12	0.14
		4.8	5.0	3.84	0.33	0.20	4.8	5.0	1.91	0.10	0.11
		5.0	5.2	3.83	0.33	0.20	5.0	5.2	2.20	0.11	0.13
		5.2	5.6	3.63	0.22	0.19	5.2	5.6	2.08	0.08	0.12
		5.6	6.0	2.64	0.21	0.14	5.6	6.0	1.80	0.07	0.10
		6.0	6.4	3.04	0.21	0.16	6.0	6.4	1.568	0.066	0.087
		6.4	6.8	2.36	0.20	0.13	6.4	6.8	1.576	0.064	0.087

Continued on next page

θ_{low}	θ_{up}	p_{low}	p_{up}	$\frac{d\sigma}{dp} \pi^+$	Δ_{stat}	Δ_{sys}	p_{low}	p_{up}	$\frac{d\sigma}{dp} \pi^-$	Δ_{stat}	Δ_{sys}
(mrad)	(GeV/c)	(GeV/c)	(GeV/c)	[mb/(GeV/c)]	[mb/(GeV/c)]	[mb/(GeV/c)]	(GeV/c)	(GeV/c)	[mb/(GeV/c)]	[mb/(GeV/c)]	[mb/(GeV/c)]
		6.8	7.2	2.27	0.13	0.12	6.8	7.2	1.264	0.058	0.069
		7.2	7.6	2.18	0.13	0.12	7.2	7.6	1.180	0.055	0.064
		7.6	8.0	1.74	0.11	0.09	7.6	8.0	1.038	0.053	0.056
		8.0	8.4	1.54	0.11	0.08	8.0	8.4	0.928	0.049	0.050
		8.4	8.8	1.48	0.11	0.08	8.4	8.8	0.894	0.048	0.047
		8.8	9.2	1.34	0.10	0.07	8.8	9.2	0.681	0.042	0.036
		9.2	9.6	1.189	0.097	0.065	9.2	9.6	0.654	0.041	0.035
		9.6	10.0	0.995	0.090	0.055	9.6	10.0	0.579	0.038	0.031
		10.0	10.8	0.870	0.057	0.048	10.0	10.8	0.481	0.024	0.025
		10.8	11.6	0.657	0.052	0.036	10.8	11.6	0.368	0.022	0.019
		11.6	12.4	0.562	0.046	0.031	11.6	12.4	0.253	0.019	0.013
		12.4	13.2	0.414	0.038	0.023	12.4	13.2	0.248	0.018	0.013
		13.2	14.0	0.260	0.032	0.015	13.2	14.0	0.147	0.014	0.008
		14.0	14.8	0.230	0.031	0.013	14.0	14.8	0.120	0.013	0.006
		14.8	15.6	0.168	0.027	0.009	14.8	15.6	0.079	0.011	0.004
		15.6	16.4	0.123	0.024	0.007	15.6	16.4	0.0598	0.0093	0.0032
		16.4	17.2	0.090	0.039	0.005					
60	100	0.2	0.3	1.25	0.11	0.13	0.2	0.3	1.28	0.10	0.22
		0.3	0.4	2.58	0.18	0.20	0.3	0.4	2.23	0.15	0.31
		0.4	0.5	3.98	0.23	0.26	0.4	0.5	3.23	0.20	0.38
		0.5	0.6	4.48	0.23	0.27	0.5	0.6	3.99	0.20	0.43
		0.6	0.7	5.86	0.26	0.34	0.6	0.7	5.02	0.23	0.50
		0.7	0.8	6.29	0.28	0.36	0.7	0.8	5.45	0.23	0.52
		0.8	0.9	7.81	0.32	0.47	0.8	0.9	5.74	0.24	0.52
		0.9	1.0	8.68	0.34	0.52	0.9	1.0	6.49	0.29	0.59
							1.0	1.2	6.90	0.21	0.58
		1.2	1.4	9.42	0.91	0.91	1.2	1.4	7.50	0.22	0.62
		1.4	1.6	11.6	1.1	1.5	1.4	1.6	8.09	0.25	0.63
		1.6	1.8	12.6	1.1	1.8	1.6	1.8	8.40	0.26	0.61
		1.8	2.0	12.41	0.79	0.85	1.8	2.0	8.78	0.26	0.61
		2.0	2.2	10.68	0.75	0.73	2.0	2.2	8.40	0.24	0.55
		2.2	2.4	12.96	0.81	0.96	2.2	2.4	9.24	0.25	0.58
		2.4	2.6	11.76	0.58	0.85	2.4	2.6	8.41	0.24	0.51
		2.6	2.8	10.25	0.73	0.62	2.6	2.8	8.24	0.24	0.49
		2.8	3.0	10.43	0.57	0.61	2.8	3.0	8.05	0.23	0.47
		3.0	3.2	10.88	0.56	0.61	3.0	3.2	7.21	0.23	0.47
		3.2	3.4	10.51	0.55	0.59	3.2	3.4	7.12	0.23	0.45
		3.4	3.6	9.34	0.48	0.51	3.4	3.6	7.03	0.23	0.44
		3.6	3.8	9.82	0.52	0.54	3.6	3.8	6.23	0.21	0.38
		3.8	4.0	8.66	0.48	0.47	3.8	4.0	6.11	0.21	0.37
		4.0	4.2	8.01	0.45	0.44	4.0	4.2	5.80	0.20	0.35
		4.2	4.4	7.90	0.46	0.43	4.2	4.4	5.32	0.20	0.32
		4.4	4.6	8.52	0.48	0.47	4.4	4.6	5.06	0.19	0.30
		4.6	4.8	6.37	0.42	0.35	4.6	4.8	4.68	0.18	0.27
		4.8	5.0	6.64	0.43	0.37	4.8	5.0	4.35	0.18	0.26
		5.0	5.2	5.60	0.39	0.31	5.0	5.2	3.92	0.17	0.23
		5.2	5.6	5.53	0.29	0.31	5.2	5.6	3.67	0.11	0.21
		5.6	6.0	5.14	0.27	0.29	5.6	6.0	3.24	0.11	0.19
		6.0	6.4	4.17	0.24	0.23	6.0	6.4	2.61	0.10	0.15
		6.4	6.8	4.00	0.24	0.22	6.4	6.8	2.18	0.09	0.12
		6.8	7.2	3.09	0.21	0.17	6.8	7.2	1.96	0.08	0.11
		7.2	7.6	3.09	0.21	0.17	7.2	7.6	1.735	0.078	0.098
		7.6	8.0	2.46	0.16	0.14	7.6	8.0	1.531	0.074	0.086
		8.0	8.4	2.06	0.17	0.12	8.0	8.4	1.100	0.063	0.062
		8.4	8.8	1.55	0.15	0.09	8.4	8.8	1.052	0.062	0.059
		8.8	9.2	1.28	0.14	0.07	8.8	9.2	0.785	0.054	0.045
		9.2	9.6	0.98	0.12	0.06	9.2	9.6	0.716	0.051	0.040
		9.6	10.0	1.04	0.12	0.06	9.6	10.0	0.584	0.047	0.033
		10.0	10.8	0.878	0.081	0.052	10.0	10.8	0.490	0.030	0.027
		10.8	11.6	0.505	0.063	0.030	10.8	11.6	0.312	0.024	0.017

Continued on next page

θ_{low}	θ_{up}	p_{low}	p_{up}	$\frac{d\sigma}{dp} \pi^+$	Δ_{stat}	Δ_{sys}	p_{low}	p_{up}	$\frac{d\sigma}{dp} \pi^-$	Δ_{stat}	Δ_{sys}
(mrad)	(GeV/c)	(GeV/c)	(GeV/c)	[mb/(GeV/c)]	[mb/(GeV/c)]	[mb/(GeV/c)]	(GeV/c)	(GeV/c)	[mb/(GeV/c)]	[mb/(GeV/c)]	[mb/(GeV/c)]
		11.6	12.4	0.270	0.054	0.016	11.6	12.4	0.194	0.020	0.011
		12.4	13.2	0.271	0.048	0.016	12.4	13.2	0.121	0.016	0.007
							13.2	14.0	0.095	0.014	0.005
100	140	0.2	0.3	2.27	0.28	0.22	0.2	0.3	1.96	0.21	0.29
		0.3	0.4	3.72	0.34	0.25	0.3	0.4	3.47	0.26	0.44
		0.4	0.5	5.95	0.37	0.35	0.4	0.5	4.92	0.29	0.50
		0.5	0.6	7.18	0.38	0.40	0.5	0.6	6.04	0.30	0.56
		0.6	0.7	8.99	0.41	0.48	0.6	0.7	8.18	0.34	0.68
		0.7	0.8	10.02	0.45	0.54	0.7	0.8	8.00	0.34	0.61
		0.8	0.9	10.96	0.49	0.63	0.8	0.9	9.28	0.37	0.67
		0.9	1.0	11.73	0.47	0.68	0.9	1.0	9.67	0.38	0.67
		1.0	1.2	13.2	0.9	1.1	1.0	1.2	10.68	0.27	0.68
		1.2	1.4	13.0	0.9	1.0	1.2	1.4	10.50	0.26	0.69
		1.4	1.6	14.4	1.0	1.1	1.4	1.6	10.52	0.25	0.59
		1.6	1.8	14.2	1.2	1.0	1.6	1.8	10.62	0.27	0.56
		1.8	2.0	12.33	0.91	0.78	1.8	2.0	10.83	0.27	0.53
		2.0	2.2	12.70	0.88	0.77	2.0	2.2	9.96	0.26	0.47
		2.2	2.4	12.74	0.87	0.76	2.2	2.4	9.74	0.24	0.43
		2.4	2.6	12.02	0.87	0.71	2.4	2.6	9.32	0.23	0.40
		2.6	2.8	9.72	0.54	0.57	2.6	2.8	8.46	0.22	0.35
		2.8	3.0	9.21	0.55	0.54	2.8	3.0	7.87	0.22	0.32
		3.0	3.2	9.26	0.54	0.55	3.0	3.2	7.39	0.23	0.40
		3.2	3.4	8.04	0.49	0.47	3.2	3.4	6.18	0.21	0.31
		3.4	3.6	7.73	0.49	0.45	3.4	3.6	6.02	0.21	0.31
		3.6	3.8	6.77	0.43	0.40	3.6	3.8	5.00	0.19	0.26
		3.8	4.0	5.46	0.38	0.32	3.8	4.0	4.74	0.18	0.24
		4.0	4.2	5.47	0.41	0.32	4.0	4.2	4.27	0.18	0.22
		4.2	4.4	5.35	0.40	0.31	4.2	4.4	3.86	0.17	0.19
		4.4	4.6	3.88	0.34	0.23	4.4	4.6	3.39	0.16	0.17
		4.6	4.8	3.87	0.35	0.23	4.6	4.8	3.13	0.15	0.15
		4.8	5.0	3.81	0.35	0.22	4.8	5.0	2.65	0.14	0.13
		5.0	5.2	3.32	0.32	0.20	5.0	5.2	2.46	0.13	0.12
		5.2	5.6	2.54	0.19	0.15	5.2	5.6	2.05	0.09	0.10
		5.6	6.0	2.64	0.19	0.16	5.6	6.0	1.645	0.077	0.081
		6.0	6.4	1.83	0.17	0.11	6.0	6.4	1.321	0.068	0.065
		6.4	6.8	1.15	0.14	0.07	6.4	6.8	1.061	0.062	0.053
		6.8	7.2	1.14	0.14	0.07	6.8	7.2	0.746	0.052	0.037
		7.2	7.6	0.86	0.12	0.05	7.2	7.6	0.593	0.048	0.029
		7.6	8.0	0.63	0.11	0.04	7.6	8.0	0.472	0.042	0.023
		8.0	8.4	0.533	0.099	0.033	8.0	8.4	0.369	0.038	0.018
		8.4	8.8	0.39	0.12	0.02	8.4	8.8	0.218	0.029	0.011
							8.8	9.2	0.188	0.029	0.009
							9.2	9.6	0.205	0.029	0.010
140	180	0.2	0.3	3.56	0.35	0.29	0.2	0.3	3.02	0.30	0.41
		0.3	0.4	6.05	0.39	0.37	0.3	0.4	4.51	0.34	0.50
		0.4	0.5	8.57	0.42	0.45	0.4	0.5	6.59	0.37	0.58
		0.5	0.6	8.91	0.42	0.45	0.5	0.6	7.72	0.39	0.62
		0.6	0.7	11.31	0.45	0.55	0.6	0.7	9.58	0.42	0.65
		0.7	0.8	13.37	0.51	0.64	0.7	0.8	10.94	0.44	0.67
		0.8	0.9	13.96	0.52	0.72	0.8	0.9	11.20	0.45	0.63
		0.9	1.0	13.34	0.50	0.69	0.9	1.0	10.82	0.43	0.59
		1.0	1.2	12.2	1.0	1.0	1.0	1.2	11.95	0.29	0.63
		1.2	1.4	12.3	1.2	1.0	1.2	1.4	12.44	0.43	0.60
		1.4	1.6	14.0	1.2	0.9	1.4	1.6	12.49	0.31	0.55
		1.6	1.8	13.8	1.2	0.9	1.6	1.8	11.04	0.28	0.42
		1.8	2.0	12.1	1.1	0.8	1.8	2.0	11.27	0.29	0.40
		2.0	2.2	12.7	1.1	0.8	2.0	2.2	9.89	0.27	0.34
		2.2	2.4	9.59	0.98	0.59	2.2	2.4	8.25	0.25	0.29
		2.4	2.6	7.65	0.79	0.48	2.4	2.6	7.46	0.24	0.25
		2.6	2.8	8.27	0.92	0.52	2.6	2.8	6.62	0.22	0.21

Continued on next page

θ_{low}	θ_{up}	p_{low}	p_{up}	$\frac{d\sigma}{dp} \pi^+$	Δ_{stat}	Δ_{sys}	p_{low}	p_{up}	$\frac{d\sigma}{dp} \pi^-$	Δ_{stat}	Δ_{sys}
(mrad)	(GeV/c)	(GeV/c)	(GeV/c)	[mb/(GeV/c)]	[mb/(GeV/c)]	[mb/(GeV/c)]	(GeV/c)	(GeV/c)	[mb/(GeV/c)]	[mb/(GeV/c)]	[mb/(GeV/c)]
		2.8	3.0	5.80	0.77	0.36	2.8	3.0	5.74	0.20	0.18
		3.0	3.2	6.04	0.78	0.38	3.0	3.2	5.24	0.19	0.24
		3.2	3.4	3.76	0.63	0.24	3.2	3.4	4.48	0.18	0.20
		3.4	3.6	4.31	0.66	0.28	3.4	3.6	3.80	0.16	0.17
		3.6	3.8	3.58	0.62	0.23	3.6	3.8	3.24	0.15	0.15
		3.8	4.0	3.05	0.57	0.19	3.8	4.0	3.02	0.15	0.14
		4.0	4.2	3.32	0.60	0.21	4.0	4.2	2.40	0.13	0.10
		4.2	4.4	3.37	0.62	0.22	4.2	4.4	2.20	0.13	0.10
		4.4	4.6	1.28	0.41	0.08	4.4	4.6	1.92	0.12	0.08
		4.6	4.8	2.05	0.49	0.13	4.6	4.8	1.58	0.11	0.07
		4.8	5.0	1.34	0.41	0.09	4.8	5.0	1.50	0.10	0.06
		5.0	5.2	1.20	0.39	0.08	5.0	5.2	1.141	0.093	0.050
		5.2	5.6	1.16	0.18	0.08	5.2	5.6	0.748	0.051	0.033
		5.6	6.0	0.83	0.16	0.05	5.6	6.0	0.661	0.049	0.028
							6.0	6.4	0.407	0.037	0.017
							6.4	6.8	0.314	0.035	0.013
							6.8	7.2	0.283	0.031	0.012
							7.2	7.6	0.223	0.030	0.009
180	240	0.2	0.3	6.73	0.38	0.48	0.2	0.3	5.61	0.31	0.71
		0.3	0.4	10.66	0.43	0.58	0.3	0.4	9.3	0.4	1.0
		0.4	0.5	15.58	0.50	0.75	0.4	0.5	13.1	0.4	1.2
		0.5	0.6	17.33	0.52	0.77	0.5	0.6	15.7	0.5	1.2
		0.6	0.7	20.03	0.54	0.84	0.6	0.7	17.7	0.5	1.2
		0.7	0.8	21.01	0.61	0.89	0.7	0.8	18.8	0.5	1.1
		0.8	0.9	22.4	0.7	1.0	0.8	0.9	19.0	0.5	1.1
		0.9	1.0	22.1	0.6	1.0	0.9	1.0	20.0	0.5	1.1
		1.0	1.2	23.0	1.6	1.7	1.0	1.2	19.3	0.4	1.1
		1.2	1.4	21.8	1.5	1.6	1.2	1.4	18.17	0.35	0.97
		1.4	1.6	18.5	1.3	1.3	1.4	1.6	16.74	0.34	0.74
		1.6	1.8	15.8	1.3	1.1	1.6	1.8	14.25	0.32	0.60
		1.8	2.0	15.2	1.2	1.0	1.8	2.0	12.50	0.29	0.50
		2.0	2.2	12.5	1.1	0.8	2.0	2.2	10.46	0.27	0.42
		2.2	2.4	11.6	1.1	0.8	2.2	2.4	9.29	0.26	0.35
		2.4	2.6	7.48	0.86	0.49	2.4	2.6	7.80	0.23	0.29
		2.6	2.8	7.62	0.86	0.49	2.6	2.8	6.63	0.21	0.24
		2.8	3.0	6.51	0.81	0.44	2.8	3.0	5.63	0.20	0.21
		3.0	3.2	5.89	0.75	0.39	3.0	3.2	4.30	0.20	0.22
		3.2	3.4	3.83	0.63	0.24	3.2	3.4	3.47	0.18	0.17
		3.4	3.6	4.95	0.66	0.33	3.4	3.6	2.80	0.16	0.14
		3.6	3.8	3.54	0.62	0.25	3.6	3.8	2.36	0.15	0.12
		3.8	4.0	2.91	0.56	0.19	3.8	4.0	1.93	0.14	0.10
		4.0	4.2	2.31	0.52	0.15	4.0	4.2	1.49	0.12	0.08
		4.2	4.4	1.74	0.46	0.12	4.2	4.4	1.49	0.12	0.07
		4.4	4.6	1.28	0.41	0.09	4.4	4.6	1.26	0.11	0.07
		4.6	4.8	1.72	0.45	0.11	4.6	4.8	1.04	0.10	0.05
							4.8	5.0	0.826	0.092	0.044
							5.0	5.2	0.593	0.076	0.032
							5.2	5.6	0.471	0.047	0.025
							5.6	6.0	0.275	0.037	0.017
							6.0	6.4	0.181	0.033	0.010
240	300	0.2	0.3	8.49	0.44	0.54	0.2	0.3	7.36	0.37	0.87
		0.3	0.4	13.98	0.53	0.66	0.3	0.4	12.4	0.4	1.2
		0.4	0.5	17.89	0.59	0.78	0.4	0.5	15.8	0.5	1.4
		0.5	0.6	20.21	0.61	0.84	0.5	0.6	17.7	0.5	1.3
		0.6	0.7	21.75	0.64	0.84	0.6	0.7	19.7	0.6	1.2
		0.7	0.8	22.60	0.71	0.91	0.7	0.8	19.4	0.6	1.1
		0.8	0.9	22.28	0.74	0.96	0.8	0.9	19.8	0.6	1.1
		0.9	1.0	22.5	1.1	0.9	0.9	1.0	18.4	1.1	0.9
		1.0	1.2	17.1	1.5	1.5	1.0	1.2	17.00	0.40	0.94
		1.2	1.4	16.0	1.5	1.3	1.2	1.4	14.82	0.37	0.77

Continued on next page

θ_{low}	θ_{up}	p_{low}	p_{up}	$\frac{d\sigma}{dp} \pi^+$	Δ_{stat}	Δ_{sys}	p_{low}	p_{up}	$\frac{d\sigma}{dp} \pi^-$	Δ_{stat}	Δ_{sys}
(mrad)	(GeV/c)	(GeV/c)	(GeV/c)	[mb/(GeV/c)]	[mb/(GeV/c)]	[mb/(GeV/c)]	(GeV/c)	(GeV/c)	[mb/(GeV/c)]	[mb/(GeV/c)]	[mb/(GeV/c)]
		1.4	1.6	14.0	1.3	1.1	1.4	1.6	12.94	0.35	0.66
		1.6	1.8	13.3	1.1	1.0	1.6	1.8	10.20	0.31	0.51
		1.8	2.0	11.7	1.4	1.0	1.8	2.0	8.32	0.28	0.41
							2.0	2.2	6.28	0.25	0.31
							2.2	2.4	5.32	0.22	0.20
							2.4	2.6	3.96	0.19	0.15
							2.6	2.8	3.15	0.17	0.12
							2.8	3.0	2.63	0.16	0.10
							3.0	3.2	2.02	0.14	0.12
							3.2	3.4	1.42	0.12	0.09
							3.4	3.6	0.963	0.095	0.057
							3.6	3.8	1.00	0.10	0.06
							3.8	4.0	0.731	0.085	0.044
							4.0	4.2	0.484	0.070	0.031
							4.2	4.4	0.368	0.060	0.023
300	360	0.2	0.3	10.16	0.69	0.52	0.2	0.3	8.29	0.56	0.98
		0.3	0.4	15.46	0.70	0.70	0.3	0.4	13.6	0.6	1.4
		0.4	0.5	18.86	0.71	0.83	0.4	0.5	16.6	0.6	1.5
		0.5	0.6	21.44	0.73	0.87	0.5	0.6	18.8	0.6	1.5
		0.6	0.7	21.50	0.73	0.82	0.6	0.7	20.0	0.7	1.5
		0.7	0.8	21.32	0.81	0.79	0.7	0.8	20.0	0.7	1.4
		0.8	0.9	20.47	0.79	0.74	0.8	0.9	17.2	0.6	1.2
		0.9	1.0	19.18	0.78	0.73	0.9	1.0	16.6	0.6	1.1
							1.0	1.2	14.02	0.41	0.89
							1.2	1.4	11.09	0.40	0.72
							1.4	1.6	7.89	0.34	0.49
							1.6	1.8	6.53	0.31	0.39
							1.8	2.0	4.25	0.24	0.26
							2.0	2.2	3.43	0.22	0.21
							2.2	2.4	2.81	0.19	0.17
							2.4	2.6	1.81	0.15	0.11
							2.6	2.8	1.31	0.13	0.08
							2.8	3.0	1.06	0.12	0.06
							3.0	3.2	0.68	0.10	0.05
							3.2	3.4	0.512	0.093	0.036
360	420	0.2	0.3	11.81	0.80	0.91	0.2	0.3	10.5	0.7	1.2
		0.3	0.4	18.3	1.0	1.3	0.3	0.4	14.1	0.8	1.5
		0.4	0.5	19.6	0.9	1.4	0.4	0.5	16.9	0.8	1.6
		0.5	0.6	18.0	0.8	1.2	0.5	0.6	18.0	0.8	1.6
		0.6	0.7	19.2	0.8	1.3	0.6	0.7	16.6	0.7	1.4
		0.7	0.8	18.1	0.9	1.2	0.7	0.8	15.7	0.7	1.3
		0.8	0.9	16.7	0.8	1.2	0.8	0.9	14.8	0.7	1.2
		0.9	1.0	15.1	0.8	1.1	0.9	1.0	11.97	0.58	0.92
							1.0	1.2	11.07	0.39	0.84
							1.2	1.4	7.76	0.36	0.60
							1.4	1.6	5.22	0.26	0.39
							1.6	1.8	4.30	0.24	0.33
							1.8	2.0	2.71	0.19	0.22
							2.0	2.2	1.80	0.16	0.13
							2.2	2.4	1.38	0.14	0.10
							2.4	2.6	0.96	0.11	0.07
							2.6	2.8	0.82	0.11	0.06
							2.8	3.0	0.636	0.096	0.049